ELSEVIER

J. Non-Newtonian Fluid Mech. 140 (2006) 23–40

Journal of
Non-Newtonian
Fluid
Mechanics

www.elsevier.com/locate/jnnfm

Influence of rheological parameters on polymer induced turbulent drag reduction

Chang-Feng Li [1], Radhakrishna Sureshkumar, Bamin Khomami *

Department of Chemical Engineering and the Center for Materials Innovation, Washington University, St. Louis, MO 63130, USA

Received 26 September 2005; received in revised form 30 December 2005; accepted 30 December 2005

Abstract

Direct numerical simulations (DNS) of polymer induced drag reduction in turbulent channel flows up to the maximum drag reduction (MDR) limit have been performed using a fully spectral method in conjunction with kinetic theory based elastic dumbbell models for the description of polymer chain dynamics. It is shown that to obtain significant levels of drag reduction large polymer chain extensibility and high Weissenberg numbers are required. In addition, it is demonstrated that to capture flow dynamics in the high drag reduction (HDR) and MDR regimes, very long computational domain lengths of the order of 10^4 wall units are required. The simulation results in turn have been used to develop a scaling that describes the interplay between rheological parameters (i.e., maximum chain extension and relaxation time) and the extent of drag reduction as a function of Reynolds number. In addition, turbulence statistics are analyzed and correlations between the polymer body force and velocity fluctuations have been developed with particular emphasis on the HDR and MDR regimes. These observations have been used to decipher the effect of polymer additives on the dynamics of the flow and drag reduction.

Keywords: Drag reduction; Dilute polymeric solutions; Turbulent channel flows; FENE-P model; Oldroyd-B model; Direct numerical simulation (DNS); Spectral techniques

1. Introduction

Turbulent flows of dilute polymeric solutions play a central role in many engineering applications such as turbulent drag reduction, fire fighting and agricultural spraying. It is well known that the addition of small amounts of soluble high molecular weight polymers to inertia-dominated, wall bounded flows gives rise to a reduction of turbulent drag. Specifically, it has been observed experimentally that polymer concentrations of $O(100)$ ppm are sufficient to reduce drag up to 70%. This phenomenon has stimulated tremendous research effort in the past 50 years. Comprehensive reviews of the early literature in this area are given in Hoyt [1], Lumley [2,3] and Virk [4].

Recent detailed experimental studies of polymer induced turbulent drag reduction have identified two distinct regimes of drag reduction (DR), which are referred to as low drag reduction (LDR) and high drag reduction (HDR) regimes [5–7]. In addition, the extent of drag reduction is bounded by a maximum drag reduction (MDR) value which is a function of the Reynolds number [8]. The LDR regime ($0 < \mathrm{DR} < 30$–40%) has similar statistical characteristics as the Newtonian flow. Specifically, the mean velocity profile remains parallel to that of Newtonian flow with an upward shift of the log-region that is enhanced as DR is increased. In addition, the streamwise velocity fluctuations are enhanced, while the transverse ones are reduced with increasing DR. However, the shapes of the root mean square (rms) profile are similar to those in Newtonian flows. In the HDR regime ($40\% < \mathrm{DR} < 60\%$), the slope of the mean velocity profile is dramatically changed as the slope of the log-law is significantly enhanced with increasing DR. In addition, the Reynolds shear stress becomes relatively small [5–7]. At MDR the Reynolds shear stress becomes extremely small and the slope of the log-law region reaches a limit known as the Virk asymptote [9].

In the past decade the development of higher-order numerical methods for viscoelastic turbulent flow simulation has made it possible to investigate turbulent drag reduction in dilute polymer solutions using kinetic theory based constitutive equations. To date, direct numerical simulations have played an important role

---

* Corresponding author. Tel.: +1 314 935 6065; fax: +1 314 935 7211.
E-mail addresses: suresh@che.wustl.edu (R. Sureshkumar), bam@che.wustl.edu (B. Khomami).

[1] Present address: School of Energy and Power Engineering, Jiangsu University, Zhenjiang, Jiangsu 212013, P.R. China.

0377-0257/$ – see front matter © 2006 Elsevier B.V. All rights reserved.
doi:10.1016/j.jnnfm.2005.12.012

in understanding the interplay between polymer chain dynamics, i.e., extensional viscosity, relaxation time and polymer stress, and flow dynamics, i.e., turbulent fluctuations and coherent structures [10–14]. Specifically, it has been shown that DR is observed when the polymer chain extension in the near wall region is significantly large. Moreover, it has been demonstrated that the extent of DR is a strong function of fluid rheology (e.g., the relaxation time and the maximum chain extensibility).

Overall, it has been shown that continuum-level simulations based on elastic dumbbell models can qualitatively predict DR and the accompanying flow modification in the LDR regime [11–17]. Specifically, the prediction of the mean velocity profile, rms velocity fluctuations and the average spacing between the streamwise streaks are in excellent qualitative agreement with experimental findings. In addition, a few DNS studies have demonstrated the enhancement of the slope in the log-law region, the formation of highly correlated and elongated streamwise low-speed streaks and the rapid reduction in the Reynolds stresses in the HDR regime as observed experimentally [7,18]. However, most of these predictions have been made with computational domains that will be shown not to be sufficiently long to accurately capture the dynamics of the flow in the HDR/MDR regime (see Section 3).

Although many of the salient features of polymer induced turbulent drag reduction have been captured by direct numerical simulations (DNS), details regarding the precise interplay between fluid rheology (i.e., maximum chain extensibility and fluid relaxation time) and extent of DR as a function of Reynolds number is still lacking. In addition, hi-fidelity direct numerical simulations in the HDR and MDR regimes have not been performed to date. Motivated by these facts, we have performed extensive spectral DNS of turbulent channel flow of dilute polymeric solutions up to the MDR asymptote in order to investigate quantitatively the coupling between fluid rheology and extent of DR.

The paper is organized as follows. In Section 2 the governing equations and the numerical procedure are presented. In Section 3 we present the results of an extensive study to ascertain the effect of the computational domain size, mesh resolution and temporal averaging span in the HDR and MDR regimes. In Section 4 the influence of solution rheology on the extent of DR and flow statistics is presented. Conclusions are presented in Section 5.

2. Governing equations, simulation technique and parameter selection

For the channel Poiseuille flow considered in this study (see Fig. 1), we chose the x-axis as the mean flow direction, i.e., the direction of the constant, externally imposed, pressure gradient and the y- and the z-axes as the wall-normal and spanwise directions respectively. We use the friction velocity, defined as $U_\tau = (\tau_w/\rho)^{1/2}$, as the velocity scale, where τ_w represents the shear stress at the wall and ρ is the density of the polymer solution. In addition, h is the half-height of the channel and h/U_τ are used as the length and time scales to non-dimensionalize the equations for the conservation of mass and momentum of an incompressible viscoelastic fluid:

$$\underline{\nabla} \cdot \underline{v} = 0 \tag{1}$$

$$\frac{\partial \underline{v}}{\partial t} + \underline{v} \cdot \underline{\nabla}\, \underline{v} = -\underline{\nabla} p + \frac{1}{Re_{\tau 0}}[\beta \nabla^2 \underline{v} + (1-\beta)\underline{\nabla} \cdot \underline{\underline{\tau}}] + \underline{e}_x \tag{2}$$

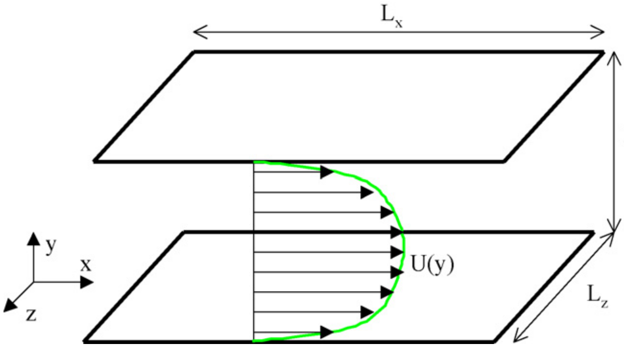

Fig. 1. Schematic of the flow geometry. L_x and L_z depict the computational domain length and width.

In the above equations, $\underline{v} = (u, v, w)$, p and $\underline{\underline{\tau}}$ denote the instantaneous values of the velocity, the excess pressure and the viscoelastic contribution to the total stress, respectively. The pressure is scaled by the wall shear stress τ_w. The last term in Eq. (2) represents the constant, mean pressure drop per unit length across the channel. The zero shear rate friction Reynolds number, $Re_{\tau 0}$, is defined as $Re_{\tau 0} = hU_\tau/\nu_0$, where ν_0 is the zero shear rate kinematic viscosity of the solution. The parameter β is the ratio of the solvent (μ_s) to the total solution zero shear-rate viscosity (μ_0), which is also a measure of polymer concentration. Finally, note that the viscoelastic stress tensor, $\underline{\underline{\tau}}$ is made dimensionless using $\mu_{p0}U_\tau/h$, where $\mu_{p0} = \mu_0 - \mu_s$ is the polymer contribution to the total zero-shear rate viscosity of solution.

Eqs. (1) and (2) are supplemented by a closed form constitutive equation for the viscoelastic stress contribution. The primary closed form constitutive equation used is the FENE-P (finitely extensible nonlinear elastic-Peterlin) dumbbell model. In this model, a polymer chain is represented by a dumbbell consisting of two beads representing the hydrodynamic resistance connected by a finitely extensible entropic spring. In addition to a polymer viscosity η_p and a relaxation time λ, this model also possesses an additional characteristic parameter L which is the maximum extensibility of the polymer chain. The choice of the FENE-P model has been motivated by the fact that it can predict the rheological properties of dilute solutions of high molecular weight polymers such as aqueous solution of polyethylene glycol (PEG) used extensively in experimental studies of polymer-induced turbulent DR with reasonable accuracy. Moreover, prior DNS studies using this model have been able to qualitatively describe the DR phenomenon and the accompanying flow modifications [11–15].

The viscoelastic stress $\underline{\underline{\tau}}$ is related to the departure of the conformation tensor $\underline{\underline{c}}$, characterizing the average second moment of the polymer chain end-to-end distance vector, from its equilibrium unit isotropic tensor state, as

$$\underline{\underline{\tau}} = \frac{f(r)\underline{\underline{c}} - \underline{\underline{I}}}{We_{\mathrm{h}}}, \quad We_h = \frac{\lambda U_\tau}{h} = \frac{\lambda U_\tau^2}{\nu_0}\frac{\nu_0}{U_\tau h} = \frac{We_\tau}{Re_{\tau 0}} \tag{3}$$

where $We_\tau = \lambda U_\tau^2/\nu_0$ is the friction Weissenberg number, a dimensionless relaxation time defined as the product of the polymer relaxation time and a characteristic shear rate based on the friction velocity. The function $f(r)$, known as the Peterlin function, is defined as

$$f(r) = \frac{L^2}{L^2 - \mathrm{trace}(\underline{\underline{c}})} \tag{4}$$

As evident from Eq. (4), $\mathrm{trace}(\underline{\underline{c}}) \leq L^2$, since as $\mathrm{trace}(\underline{\underline{c}})$ approaches L^2, the force required for further extension approaches infinity. Note that $\underline{\underline{c}}$ and L^2 are made dimensionless with respect to kT/H^*, where k, T and H^* denote the Boltzmann constant, the absolute temperature and the Hookean dumbbell spring constant, respectively.

Moreover, an Oldroyd-B model has also been used to describe the solution rheology. In the limit of $L \to \infty$, the Oldroyd-B model is obtained from the above FENE-P model with the Peterlin function simplified as,

$$f(r) = 1 \tag{4a}$$

The viscoelastic tensor is obtained by solving an evolution equation for the conformation tensor $\underline{\underline{c}}$,

$$\frac{\partial \underline{\underline{c}}}{\partial t} + \underline{v} \cdot \underline{\nabla}\underline{\underline{c}} - [\underline{\underline{c}} \cdot \underline{\nabla}\,\underline{v} + (\underline{\nabla}\,\underline{v})^{\mathrm{T}} \cdot \underline{\underline{c}}] - D\nabla^2\underline{\underline{c}} = -\underline{\underline{\tau}} \tag{5}$$

As shown by Sureshkumar and Beris [10] and later by other investigations [14,19,20] to perform stable numerical integration of the evolution equation for the conformation tensor in turbulent channel flows, it is necessary to introduce a numerical diffusivity term $D\nabla^2\underline{\underline{c}}$. In this expression D is a dimensionless number (equivalent to the inverse of a Schmidt number) defined as $D = \kappa/hU_\tau$, where κ denotes a constant isotropic artificial numerical diffusivity. In spectral methods a global artificial diffusivity (GAD) is commonly used to ensure numerical stability. However, recently local artificial diffusivity (LAD) has been applied in compact finite difference algorithms [19,20] to minimize the effect of the added artificial stress diffusion on the DNS results in lower (compared to spectral) order methods. In the LAD scheme artificial diffusivity is applied only at locations where the conformation tensor $\underline{\underline{c}}$ experiences a loss of positiveness (i.e., $D_{\mathrm{LAD}} = D_{\mathrm{GAD}}$, when $\det(\underline{\underline{c}}) \leq 0$, otherwise it set to zero). Both global and local artificial diffusivities have been implemented in the present study. The value of the numerical diffusivity is optimized so that it is large enough for the calculations to ensure numerical stability and the results for the conformation tensor is physically meaningful while small enough so that it does not affect the computational results appreciably. As pointed out by earlier studies [10–13], the artificial numerical diffusivity D was taken to be of $O(10^{-2})$ resulting in a numerical Schmidt number $\mathrm{Sc}^+ (=1/Re_{\tau 0}D)$ of the order $O(10^{-1})$.

As shown above, the flow and polymer stress fields can be fully characterized by four dimensionless groups, namely, Re_τ, β, L and We_τ. Since one of the primary objectives of this study is to investigate how these parameters influence the extent of drag reduction, in what follows, we briefly outline our rationale for the selection of the simulation parameters.

Recent computations by Housiadas and Beris [13] have shown that the extent of DR is relatively insensitive to Re_τ ($125 < Re_\tau < 590$) and DR $\leq 30\%$ in the LDR regime. However, considering the fact that viscoelastic effects in inertial flows are related to the *elasticity number* $E = We_\tau/Re_\tau{}^2$, it is reasonable to expect that Re_τ effects could be more pronounced at higher Re_τ and higher levels of drag reduction (i.e., the MDR limit increases from 69% at $Re_\tau = 125$ to 80% for $Re_\tau \geq 600$ [4]). Hence, simulations have been performed in this study with $Re_\tau = 125$, 180 and 395. Although these Reynolds numbers are still relatively small in comparison to most experimental studies of polymer induced turbulent DR, earlier studies [11,12] have shown that a sustainable fully turbulent flow can be obtained for a Newtonian fluid at $Re_\tau = 125$ (i.e., a mean Reynolds number $Re_{\mathrm{mean}} = U_{\mathrm{m}}h/\nu_0 = 1840$, where U_{m} is the mean flow). Moreover, it should be noted that DR in dilute polymer solutions has been experimentally observed at Re_{mean} as low as 8900 (i.e., $Re_\tau \sim 500$) [24].

The value of β is inversely related to the polymer concentration. Since most prior DNS studies of polymer induced turbulent DR have been performed at $Re_{\mathrm{mean}} < 8900$, they have used lower β values than those in the experiments to amplify elastic effects. In fact, β values as low as 0.4 have been used [7] in order to reach the HDR regime. However, such β values lead to significant shear thinning of the viscosity, and special care should be taken to define DR accurately. Hence, we have chosen $\beta = 0.9$ to perform our simulations as it has been shown that with this value one can capture elastic effects with negligible influence of shear-thinning viscosity (i.e., in the order of few percent) [11–13].

One of the main proposed mechanisms for polymer induced drag reduction is based on polymer molecules experiencing coil-stretch transition, causing a dramatic increase in the elongational viscosity of the solution, which in turn suppresses Reynolds stress production. The extensional viscosity of a polymer solution is a function of the polymer relaxation time and the strength of the flow as characterized by, We_τ, and the maximum extensibility of the macromolecule, L. Specifically, for the FENE-P model the Trouton ratio (i.e., the ratio of the extensional to the zero-shear rate polymer viscosity) increases from 3 at low extension rates (the Newtonian value) to $2L^2$ at high extensional rates [23]. Hence, we have performed an extensive parametric study by varying L^2 and We_τ to ascertain the influence of polymer chain dynamics on the extent of DR and the flow field.

Eqs. (1)–(5) along with the no-slip boundary conditions for the velocity on the channel walls are subsequently solved numerically using a fully spectral code (i.e., Chebyshev polynomials in wall normal y-direction and Fourier series in periodic x-and z-directions). The numerical procedure (i.e., operator splitting/influence matrix algorithm) used for the time-integration of Eqs. (1)–(5) with global artificial diffusivity (GAD) can be found in [11–13]. In addition, this algorithm has been extended to allow for the use of local artificial diffusivity (LAD). Specifically, when using LAD, the conformation tensor is calculated without artificial diffusivity, however, if at any point in the computational domain det($\underline{\underline{c}}$) is less than zero, the entire conformation tensor (i.e., at all points) is recomputed in the Fourier space with the addition of artificial diffusivity. In turn, when converting the results to the physical space only the points at which the violations have occurred (i.e., det($\underline{\underline{c}}$) < 0) are updated. This procedure is repeated until spatially converged values are obtained at each time step (i.e., a tolerance of 10^{-4} is used). It should be noted that since our approximating functions do not have compact support this implementation is not strictly equivalent to the local artificial diffusivity scheme used in the compact finite difference formulation of Dubief et al. [20].

The simulations reported in this study have been mostly performed on 16-nodes of a SGI Origin 2000 system. Typical CPU times for one eddy turnover time at $Re_\tau = 395$ (grids in $128 \times 129 \times 64$, $\mathrm{d}t = 1 \times 10^{-4}$) is approximately 10.

3. Effect of the computational domain size, mesh resolution and artificial diffusivity

It is a well known fact that in wall bounded turbulent flows of dilute polymeric solutions the streamwise and spanwise scales are larger than those for a typical Newtonian flow due to the coarsening of near-wall structures [24–27]. It has also been experimentally shown that the streamwise coherence could be increased by an order of magnitude over the Newtonian length scale (i.e., $l^+ = lU_\tau/\nu$ of $O(1000)$). Hence, the selection of computational domain size and time averaging span plays a central role in determining the fidelity of DNS results for polymeric systems. To date, a number of spectral DNS studies [11–13] have shown that for $Re_\tau = 125$ a computational domain size of $10h \times 2h \times 5h$ ($1250 \times 250 \times 625$ in wall units) in x, y, z-directions respectively with a spatial discretization of $64 \times 65 \times 64$ is adequate to capture the streamwise and spanwise structures for DR up to 30% (i.e., the LDR regime). Specially, it has been shown that the two-point correlations in the streamwise and the spanwise directions reduce to essentially zero at maximum separation (half of the domain size). In addition, it has been demonstrated that temporal averaging over 10–15 eddy turnover times is sufficient to obtain good statistics in the LDR regime. To date, extensive studies of how domain size and temporal and spatial discretization influence the accuracy of DNS results at high levels of DR (i.e., HDR and MDR) are lacking. Hence, we have performed a systematic study on the effect of computational domain size, spatial discretization and time averaging span on the flow field in the HDR and MDR regimes.

Fig. 2 shows the effect of computational domain size in the HDR regime ($Re_\tau = 125$, $We_\tau = 100$, $L^2 = 3600$). In Fig. 2a, the temporal evolution of the mean flow Reynolds number and the percentage of drag reduction (%DR) are presented. Note that the same numerical resolution (i.e., Δx^+, Δy^+ and Δz^+) is used for all the cases reported. For example, the number of nodes in the flow direction is increased from 64 to 384 as the computational domain size along the flow direction is increased from $10h$ to $60h$. These results clearly show that the computational domain size influences the predicted extent of DR in the HDR regime. Specially, it is observed that domain sizes less than $20h \times 2h \times 5h$ are insufficient for obtaining accurate prediction of DR. In fact, in small domains such as $5h \times 2h \times 5h$, a higher level of DR (≈10%) is predicted than those in the longer domains. This is attributed to the fact that the periodic boundary conditions in the shorter domains do not allow all the larger scales to be captured.

A more rigorous test of determining the adequacy of the domain size is provided by the two-point streamwise correlations R_{uu} in the buffer layer where the elastic effects are most prominent (see Fig. 2b). As evinced by Fig. 2b, the coefficients of R_{uu} have large value in the two small domains, which indicates that some of the largest turbulence scales have not been fully captured. Specifically, in the smallest domain $5h \times 2h \times 5h$, R_{uu} is larger than 0.95 at the maximum separation, showing that most of the streamwise turbulence scales are longer than the domain size. With the increase in the computational domain length, larger turbulence scales are progressively captured and the velocity becomes less correlated. In the three longest domains R_{uu} drops much faster than those in the small domains. In addition, the final correlation values are acceptable (i.e., in the longest domain the correlation drops to zero at the maximum separation). This analysis clearly suggests that very long streamwise structures exist in the flow in the HDR regime. Hence, to adequately capture dynamical events and obtain an accurate measure of the energy at the longest wavelength, large simulation boxes with length of approximately $100h$ are required. However, to obtain reasonable statistics for many quantities of interest such as %DR, velocity and vorticity fluctuations and polymer stretch, a relatively modest box size of the order $20h$ is sufficient. Specifically, the %DR obtained from DNS using a $20h$ box (${L_x}^+ = 2500$) only differs by 4% from that from the $80h$ box (${L_x}^+ = 10{,}000$).

The effect of the computational domain size in the MDR regime ($Re_\tau = 125$, $We_\tau = 100$, $L^2 = 14{,}400$) is shown in Fig. 3. Once again, it can be seen that at MDR much longer computational domains are required than in the LDR regime. Specifically, it is observed that in the domain $20h \times 2h \times 5h$ the flow is entirely laminarized. However, turbulence can be sustained in the longer domains of $40h \times 2h \times 5h$ and $60h \times 2h \times 5h$ with drag reduction level of $74 \pm 2\%$. The two-point streamwise correlations R_{uu} in the MDR regime are shown in Fig. 3b. This figure demonstrates that to adequately capture dynamical events elongated box sizes of order $120h$ are required. However, reasonable statistics for %DR and rms velocities can be obtained with box size of order $40h$ (${L_x}^+ = 5000$). Specifically, the %DR in a $40h$ box is within 2% of those obtained by using longer box sizes (80 and $120h$).

The streamwise vorticity fluctuation correlation $R_{\omega_x\omega_x}$ in the buffer layer is also shown in Fig. 3b, demonstrating the rapid decay of the two-point correlation of this quantity. For comparison, the correlations corresponding to the Newtonian flow in the buffer layer have also been plotted. It can be seen that the loss of spatial correlation is much slower at MDR than that in the Newtonian flows. Specifically, the zero-correlation separations are much farther apart than in Newtonian flows. This clearly illustrates that the larger turbulence scales become even larger

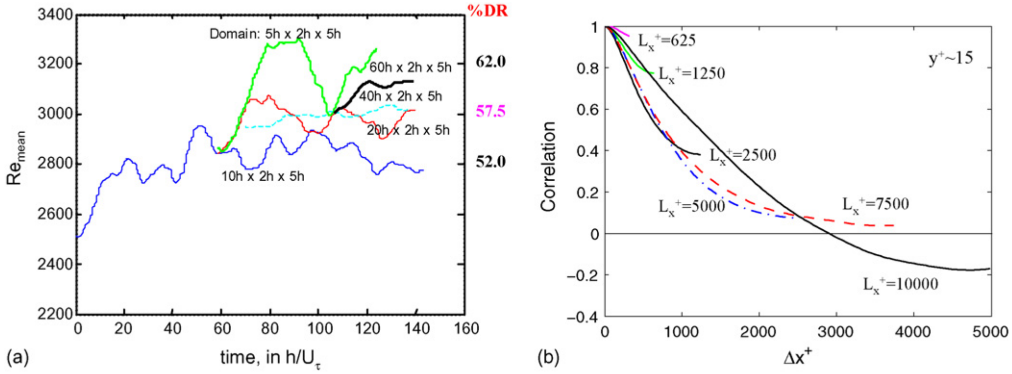

Fig. 2. The influence of domain size on computed results in the HDR regime. (a) Time evolution of the mean Reynolds number and %DR; (b) streamwise two-point correlations (i.e., R_{uu}) in the buffer layer.

with increasing DR, especially in the MDR regime where the streamwise structures are much more elongated than in Newtonian flows. Note that $R_{\omega_x\omega_x}$ always drop faster than R_{uu}, and the zero-correlation separations for $R_{\omega_x\omega_x}$ are much smaller than that in R_{uu}. This clearly shows that the streamwise vortex length scales are smaller than the velocity streak lengths. This is consistent with the fact that R_{vv} and R_{ww} are always less correlated than R_{uu} (i.e., the streamwise vorticity fluctuation is mainly due to the velocity fluctuation in v- and w-components).

Fig. 3c shows the one-dimensional power spectrum density (PSD) associated with the streamwise velocity fluctuations in two computational domains with $L_x{}^+ = 5000$ and 15,000 at MDR. A spectral gap in the PSD profile can be observed in the domain with $L_x{}^+ = 5000$, while the energy is transferred from low wavenumber (large wavelength) to high wavenumber (small wavelength) smoothly in the longer domain with $L_x{}^+ = 15{,}000$ that is capable of capturing dynamic events. This clearly shows that in order to capture the energy associated with large wavelength structures as well as the energy cascade large domain lengths are required.

Fig. 3d shows typical two-point correlations of streamwise velocity R_{uu} in the spanwise direction in the MDR regime. It can be seen that the spanwise domain width is sufficiently large as the spanwise two-point correlations all have several extrema within the half domain width (∼310 wall units). Hence, 5h (625 wall units) is sufficient to capture the structures in the spanwise direction for all DRs. Therefore, in all of our simulations we have utilized $L_z{}^+ = 625$ as our domain width.

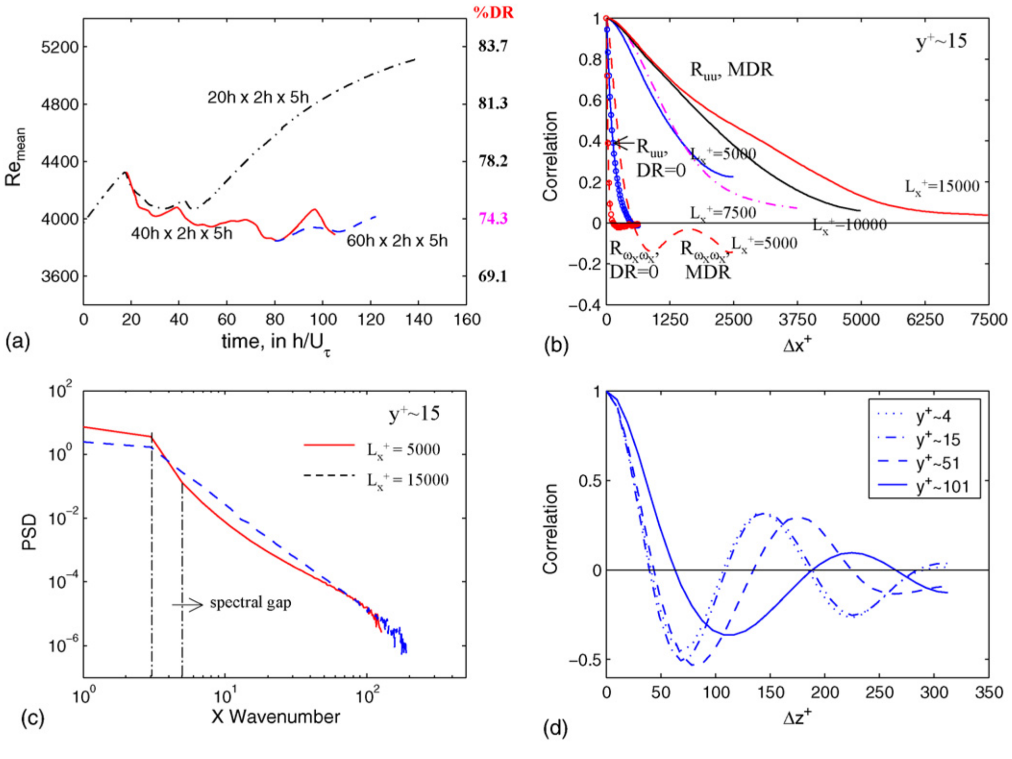

Fig. 3. The influence of domain size on computed results in the MDR regime. (a) Time evolution of the mean flow Reynolds number and %DR; (b) streamwise two-point correlations (i.e., R_{uu} and $R_{\omega_x\omega_x}$) in the buffer layer; (c) the one-dimensional power spectrum density (PSD) vs. the streamwise wavenumber for the streamwise velocity fluctuations in the buffer layer; (d) spanwise two-point correlations (i.e., R_{uu}) at several wall normal distance in the MDR regime.

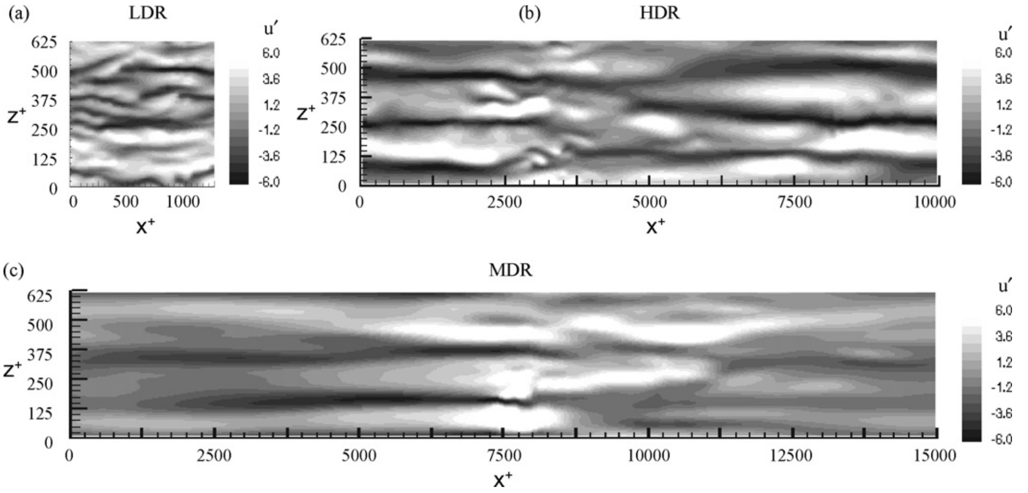

Fig. 4. Representative snapshots of velocity streaks in the $x-z$ plane at $y^+ \sim 15$ in (a) LDR; (b) HDR; (c) MDR regimes.

Usually the average streak spacing can be evaluated as twice the distance from the origin of the first minima in the spanwise two-point correlation. It can be seen that at MDR the average streak spacing is an increasing function of distance from the wall (y^+) (see Fig. 3c). Specifically, it can be seen that in the region ($y^+ \leq 100$), the streak spacing is significantly enhanced in comparison to that in Newtonian flows which is approximately 100 wall units. However, it is difficult to predict an average value for the streak spacing, since it changes greatly with the distance from the wall. For example, it can be seen that at $y^+ = 4$, 15 and 51 the first minima are approximately located at $\Delta z^+ = 75$ and 85 respectively, while at $y^+ = 101$, $\Delta z^+ = 110$. This implies that the averaging streak spacing is approximately 150, 170 and 220 at $y^+ \approx 15$, 51 and 101, respectively. These rapid changes in the streak spacing as a function of y^+ at MDR is a consequence of significant enlargement of the buffer layer. This is not the case at LDR, hence the degree of drag reduction can be well correlated to the increased streak spacing in the buffer layer [22,24].

Instantaneous streaky structures are shown in Fig. 4, demonstrating the increased streak spacing as DR is increased. In highly drag reduced flows (i.e., HDR and MDR regimes) highly organized low-speed streaks are observed. Existence of these structures necessities the use of very long domains to capture them, i.e., $L_x{}^+ \geq 10{,}000$ in the HDR regime and $L_x{}^+ \geq 15{,}000$ in the MDR regime as reported above.

We have also examined the influence of spatial discretization and artificial diffusivity on important flow quantities, such as %DR, rms velocities and polymer stretch (see Fig. 5). Our results clearly show that $\Delta x^+ \approx 40$, $\Delta z^+ \approx 10$ and $(\Delta y^+)_{\min} \approx 0.1$ are sufficient for obtaining good statistics for these quantities. However, in the HDR/MDR regime to accurately capture the gradient of polymer stretch near the wall, $(\Delta y^+)_{\min} \leq 0.06$ is required. Moreover, small levels of artificial diffusivity used in the simulations do not significantly influence the above quantities.

As mentioned earlier, simulations have been performed with both LAD and GAD schemes. The comparison of time evolution of drag reduction in LDR and HDR regimes is shown in Fig. 6. The computed average %DR is almost independent of the scheme utilized at HDR where updates (i.e., addition of diffusivity) are performed at approximately 1% of the nodes. The difference is slightly more pronounced at LDR (i.e., up to 4%) where updates are performed at approximately 40% of the nodes. Overall, our studies indicate that similar statistics for %DR, rms velocities and polymer stretch (see Fig. 6b and c) are obtained with the GAD and the LAD schemes, further underlining the negligible influence of added diffusivity in the computed results.

Taking into consideration all of the above findings, most of the results reported in the remainder of this paper are based on the following domain size and spatial discretization. In the LDR regime ($0 < \text{DR} < 30\%$), the computational domain sizes (in wall units) in the streamwise and spanwise direction are $L_x{}^+ \times L_z{}^+ = 1250 \times 625$. In the HDR ($30\% < \text{DR} < 60\%$) and MDR regimes, $L_x{}^+ \times L_z{}^+ = 2500 \times 625$ and 5000×625 are used, respectively. The uniform mesh resolution is $\Delta x^+ \approx 20$ in the LDR and HDR regimes, while $\Delta x^+ \approx 40$ is used at MDR; $\Delta z^+ \approx 10$ and $\Delta y^+ \approx 0.06$ near the wall (the Chebyshev node spacing is non-uniform in the y-direction, i.e., it is much more refined in the near wall region) are required. Simulation details are summarized in Table 1.

4. Results and discussion

4.1. Turbulent Fluctuations at HDR and MDR

Typical snapshots of xz-plane averaged quantities of interest such as Re_{mean}, rms velocities, overall momentum balance and trace($\underline{c}$) in the LDR and MDR regimes are shown in Figs. 7 and 8. A comparison of various quantities at different times clearly shows the high level of turbulent fluctuation with respect to the mean value in the MDR regime. Specifically, the variations in the xz-plane averaged data are relatively minor at LDR (i.e., time averaging over 10–15 computational units (h/U_τ) is sufficient to obtain good statistics). While, in the HDR and MDR regimes significant variations are observed. Hence, averaging over 30–50h/U_τ is needed to obtain good statistics.

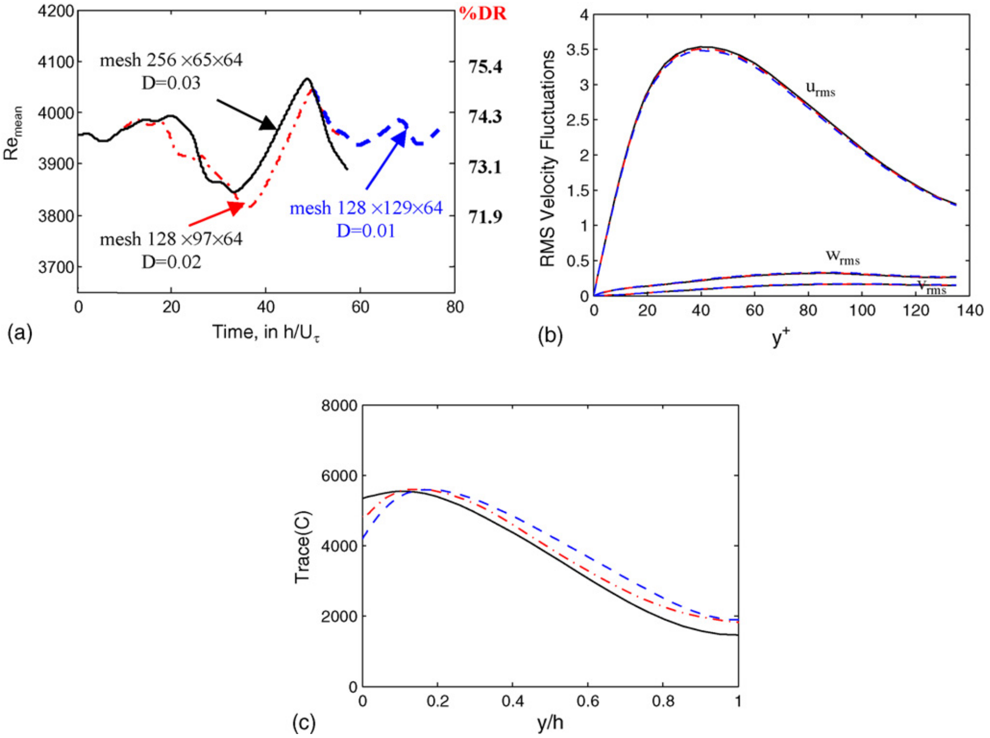

Fig. 5. Influence of spatial discretization and artificial diffusivity on important flow quantities at MDR. (a) %DR; (b) rms velocities; (c) trace($\underline{\underline{c}}$). (—) mesh $256 \times 65 \times 64$, $D = 0.03$; (-·-·-) mesh $128 \times 97 \times 64$, $D = 0.02$; (- - -) mesh $128 \times 129 \times 64$, $D = 0.01$.

4.2. Turbulence statistics

4.2.1. Mean velocity and percentage drag reduction

Since the simulations are performed with a constant pressure gradient, %DR is manifested via an increase in the flow rate (i.e., an increase in Re_{mean}). Recently, Housiadas and Beris [28] proposed the following relationship between %DR and Re_{mean} for dilute polymeric solutions with a shear rate dependent viscosity (i.e., the FENE-P model):

$$\mathrm{DR} = 1 - \mu_{\mathrm{w}}^{2(1-n)/n} \left(\frac{Re_{\text{mean}}^{\text{visc}}}{Re_{\text{mean}}^{\text{Newt}}} \right)_{Re_{\tau 0}}^{-2/n} \tag{6}$$

where μ_{w} is the effective wall viscosity, and $n = 1.1478$. Utilizing this relationship we have computed %DR as a factor of L^2, We_τ and Re_τ (see Table 2). Our results indicate that, at a

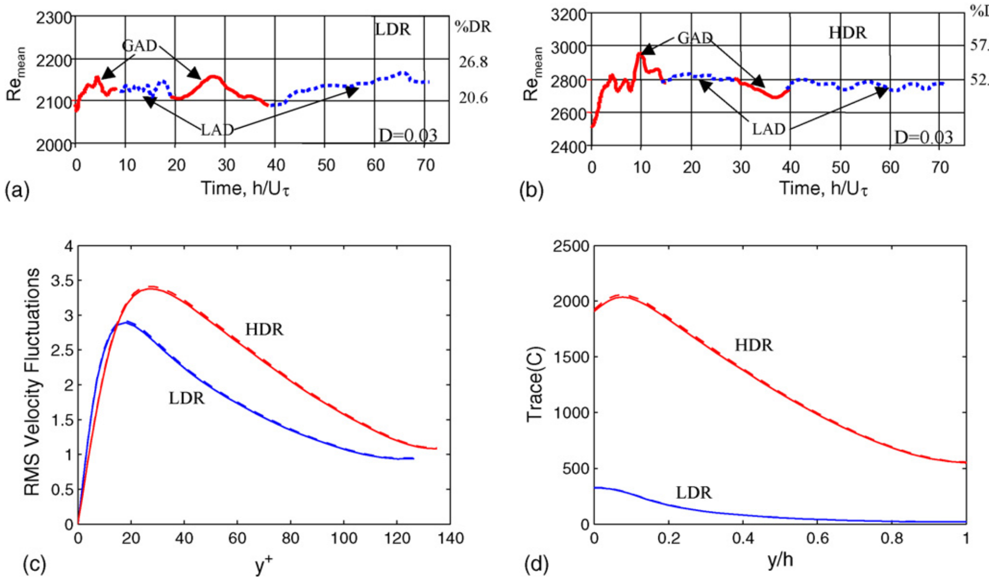

Fig. 6. Comparison of computed results utilizing the GAD and LAD schemes. (a) %DR in the LDR regime ($We_\tau = 25$, FENE-P, $L^2 = 3600$); (b) %DR in the HDR regime ($We_\tau = 100$, FENE-P, $L^2 = 3600$); (c) rms velocities; (d) trace($\underline{\underline{c}}$). (—) GAD scheme; (-·-·-) LAD scheme.

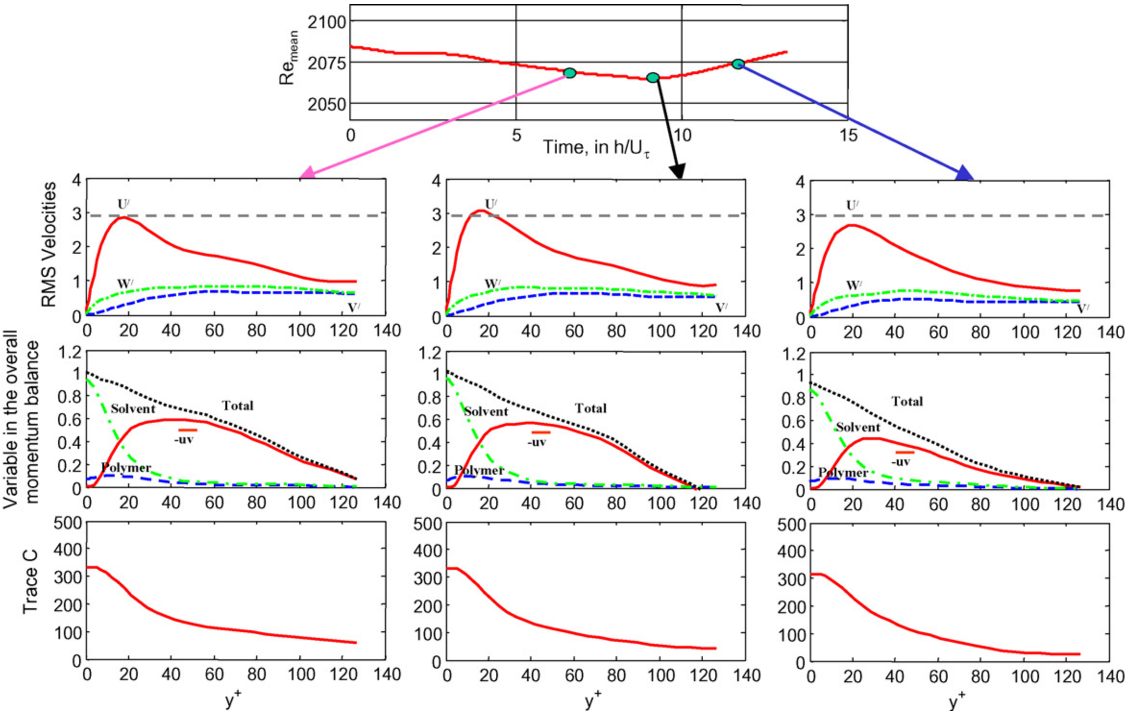

Fig. 7. Typical snapshots of *xz*-plane averaged quantities in the LDR regime.

Table 1
Simulation details

Re_τ	Parameters	Regime		
		LDR	HDR	MDR
125	Domain size (wall units)	L_x: 5h, 10h, 20h (625, 1250, 2500); L_y: 2h (250); L_z: 5h (625)	L_x: 10h, 20h, 40h, 60h, 80h (1250, 2500,5000,7500, 10000); L_y: 2h (250); L_z: 5h (625)	L_x: 20h, 40h, 60h, 80h, 120h (2500, 5000, 7500, 10000, 15000) L_y: 2h (250); L_z: 5h (625)
	Nodes	64 × 65 × 64, 128 × 65 × 64	128 × 65 × 64, 256 × 65 × 64 384 × 65 × 64, 128 × 97 × 64	128 × 65 × 64, 256 × 65 × 64, 384 × 65 × 64, 128 × 97 × 64, 128 × 129 × 64
	Δx^+, Δy^+, Δz^+	∼(10–20) × (0.15–6) × 10	∼(10–40) × (0.07–6) × 10	∼(10–40) × (0.04–6) × 10
	Δt	5 × 10^{-4}	(2–5) × 10^{-4}	(1–2) × 10^{-4}
	Artificial diffusivity	0.03	0.02–0.03	0.01–0.03
180	Domain size (wall units)	6.944h × 2h × 3472h (1250 × 360 × 625)	13.888h × 2h × 3472h (2500 × 360 × 625)	27.776h × 2h × 3472h (5000 × 360 × 625)
	Nodes	64 × 97 × 64	64 × 97 × 64, 128 × 97 × 64	128 × 97 × 64
	Δx^+, Δy^+, Δz^+	∼20 × (0.10–6) × 10	∼(20–40) × (0.10–6) × 10	∼40 × (0.10–6) × 10
	Δt	(2–5) × 10^{-4}	(1–2) × 10^{-4}	(1–2) × 10^{-4}
	Artificial diffusivity	0.02	0.02	0.02
395	Domain size (wall units)	2πh × 2h × 0.5πh (2482 × 790 × 620) 2πh × 2h × π (2482 × 790 × 1241)	2πh × 2h × 0.5πh (2482 × 790 × 620 4πh × 2h × 05πh (4964 × 790 × 620)	4πh × 2h × 0.5πh (4964 × 790 × 620)
	Nodes	128 × 129 × 64, 128 × 129 × 128	128 × 129 × 64, 256 × 129 × 128	128 × 129 × 64, 256 × 129 × 64 128 × 193 × 64
	Δx^+, Δy^+, Δz^+	∼20 × (0.12–10) × 10	∼(20–40) × (0.12–10) × 10	∼(20–40) × (0.05–10) × 10
	Δt	(2–5) × 10^{-4}	(1–2) × 10^{-4}	(1–2) × 10^{-4}
	Artificial diffusivity	0.01	0.01–0.02	0.01–0.02

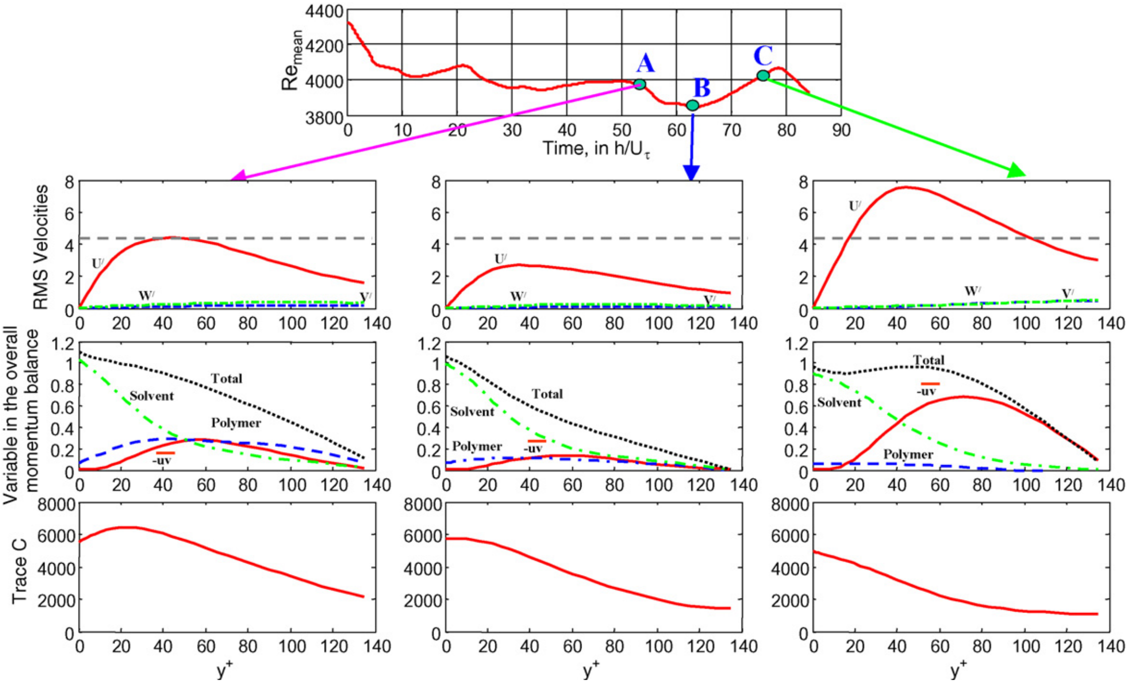

Fig. 8. Typical snapshots of *xz*-plane averaged quantities in the MDR regime.

given Re_τ, as We_τ in enhanced for a given L, %DR reaches an asymptote. Moreover, as L is increased the extent of %DR is enhanced. However, it should be noted that as proposed earlier in the HDR and MDR regimes the computed %DR at given values of L^2 and We_τ shows a dependence on Re_τ (i.e., at $We_\tau = 100$ and $L^2 = 14{,}400$, %DR = 74 for $Re_\tau = 125$, while it is 71% for $Re_\tau = 180$, and 61% for $Re_\tau = 395$). These trends are consistent with the hypothesis that the extent of DR is proportional to the extensional thickening of the dilute polymeric solution.

In order to further illustrate this point, the average trace of the polymer conformation tensor as a function of chain extensibility L, We_τ and Re_τ is depicted in Fig. 9. Clearly, as the chain length is enhanced, trace($\underline{\underline{c}}$) monotonically increases at a fixed Re_τ and We_τ. However, the percent increase in the chain length is decreased (i.e.,trace($\underline{\underline{c}}$)/$L^2$ decreased). Further note that at high Re_τ (i.e., 180 and 395) the region of high chain extension is limited to the near wall region $y/h < 0.2$. However, at $Re_\tau = 125$ significant chain extension can be observed up to $y/h \sim 0.5$ particularly in the HDR and MDR regimes. This suggests that at this Re_τ the flow is wall dominated and perhaps this value of Re_τ is too low for a comprehensive investigation of polymer induced DR at HDR and MDR. This issue will be discussed further in this section as well as in Sections 4.3 and 4.4.

Table 2
The percentage drag reduction (%DR) as a function of Re_τ, We_τ and L

Re_τ	L^2	We_τ			
		25	50	100	200
125	14	–	–	3.0	–
	56	–	–	8.0	–
	225	–	–	23.5	–
	450	–	–	31.5	–
	900	18.5	31.0	37.0	–
	1800	20.2	34.5	44.5	–
	3600	21.5	43.0	56.5	–
	7200	22.5	49.0	69.0	–
	14400	24.0	51.5	74.0	–
180	900	19.0	30.5	38.5	–
	3600	–	–	54.0	–
	14400	–	–	71.0	–
395	900	18.5	30.5	37.0	–
	3600	–	38.0	48.0	–
	14400	–	–	61.0	75.0

Typical mean streamwise velocity profiles as a function of the distance from the wall in logarithmic scale in the LDR, HDR and MDR regimes are shown in Fig. 10. For the sake of comparison the profiles for Newtonian flow at each Reynolds number have also been included. For the Newtonian cases, excellent agreement with the linear distribution $U^+ = y^+$ in the viscous sublayer, and well as the logarithmic layer $U^+ = 2.5\ln(y^+) + 5.5$ is observed. In drag reduced flows, it can be seen that all profiles in the viscous sublayer also collapse on the linear distribution $U^+ = y^+$. Further away from the wall the mean velocity of the drag reduced flows increases as compared to that in Newtonian flows. Specifically in the LDR regime, the logarithmic profile is shifted upwards parallel to that of the Newtonian flow. The same behavior is found for the mean streamwise velocity profile in the LDR regime in the channel flow experiments of Warholic et al. [5] and in earlier DNS studies [11–14]. The upward shift of the logarithmic profile can be interpreted as a thickening of the buffer layer [2,3].

In the HDR regime, the slope of the mean velocity is augmented. In addition, the slope increase is a function of %DR. In fact, at $Re_\tau = 180$ and 395 the Virk maximum asymptote is observed at 71% and 75%, respectively. Present simulations at

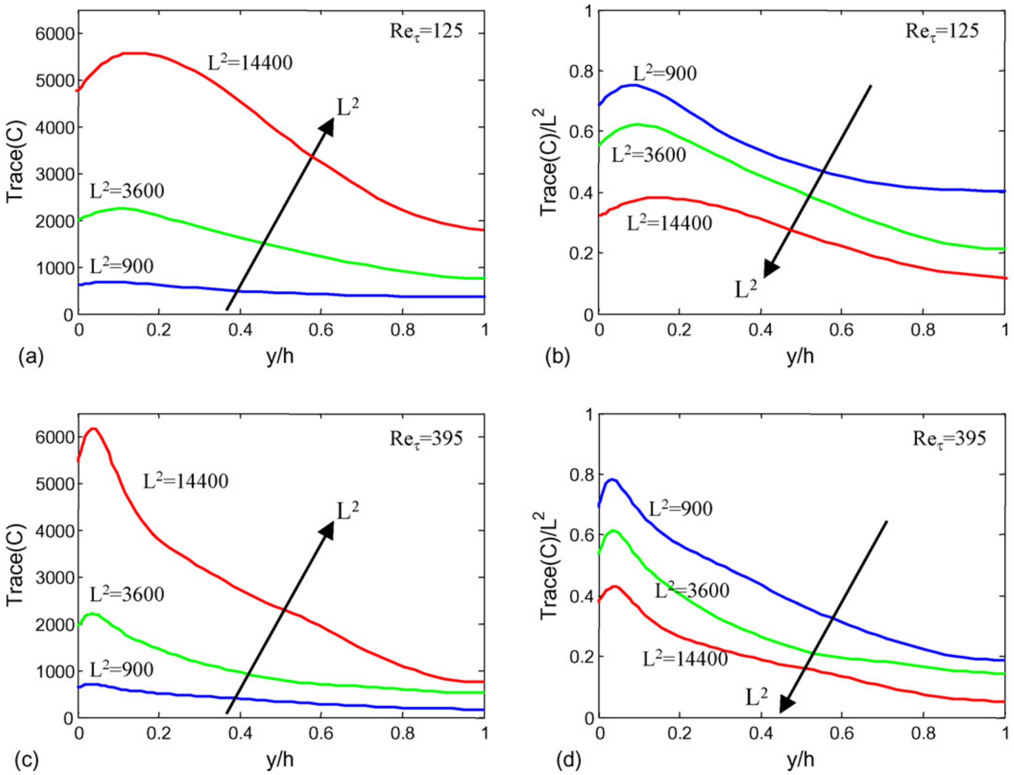

Fig. 9. Trace of the conformation tensor as a function of wall normal distance at $We_\tau = 100$.

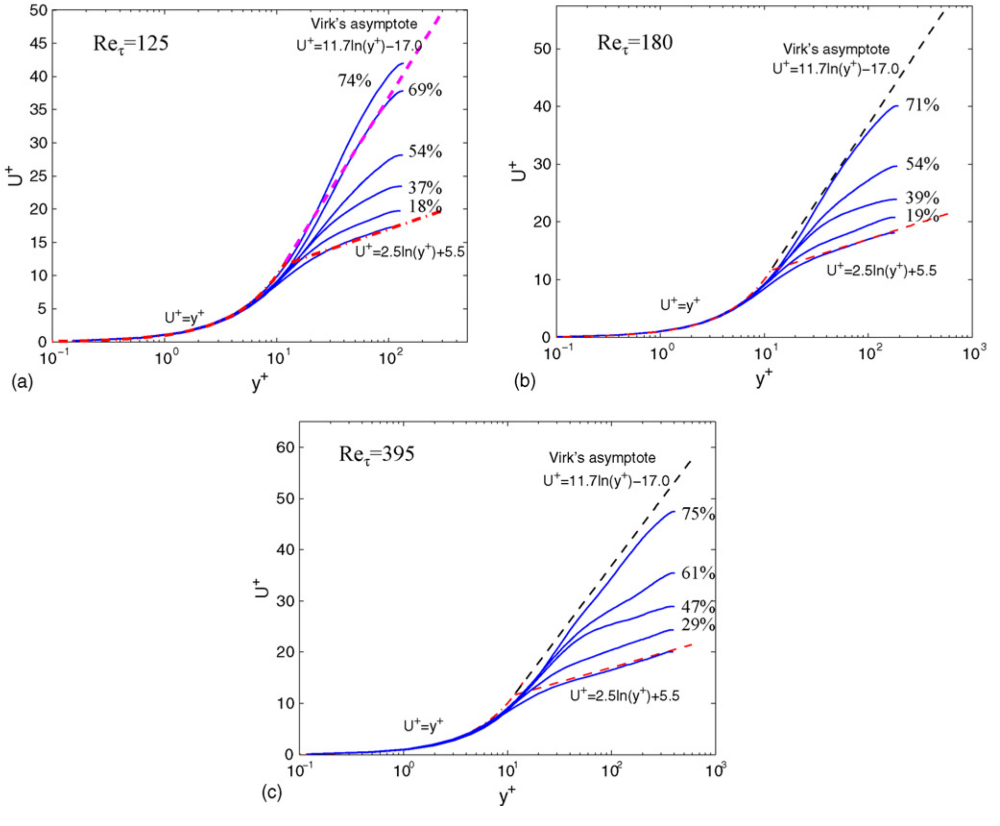

Fig. 10. Mean streamwise velocity profiles as a function of distance from the wall. (a) $Re_\tau = 125$; (b) $Re_\tau = 180$; (c) $Re_\tau = 395$.

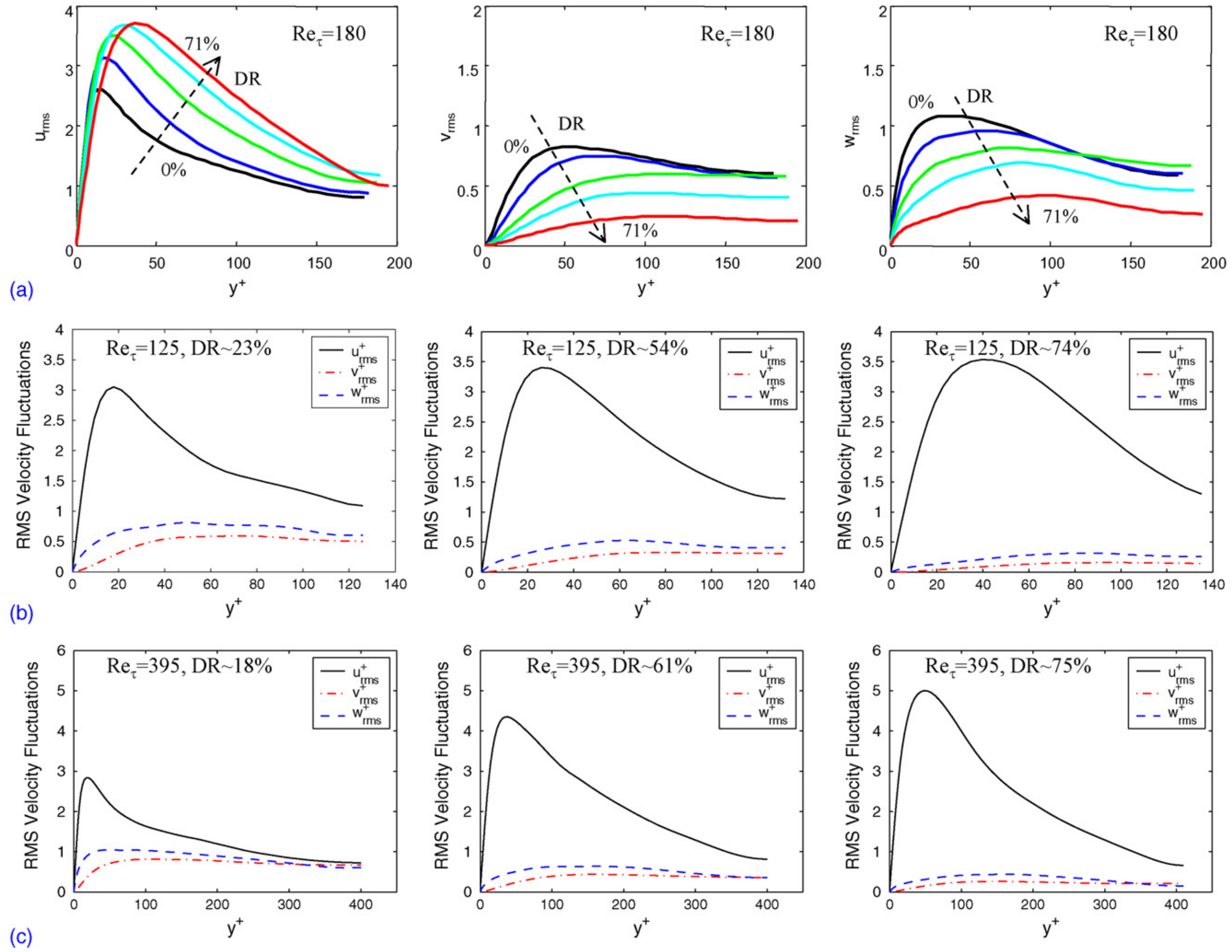

Fig. 11. The rms velocity fluctuations as a function of the distance from the wall. (a) $Re_\tau = 180$ (%DR from 0%, 19%, 39%, 54%, to 71%); (b) $Re_\tau = 125$; (c) $Re_\tau = 395$.

$Re_\tau = 125$ indicates that for $L^2 = 14{,}400$ and with the Oldyold-B model, the mean velocity profile in the center exceeds the predicted maximum value by Virk asymptote. This effect was also noted in the experimental study by Ptasinski et al. [6]. As mentioned earlier, at $Re_\tau = 125$ the flow is wall dominated at HDR and MDR. Hence, the computed results are not expected to exactly follow Virk's data [4,8] collected at much higher Re_τ where the flow is not wall dominated.

4.2.2. Velocity fluctuations

The rms of three velocity component fluctuations for drag reduced flows along with Newtonian data are shown in Fig. 11. It is well known [5,22,24,25] that in the LDR regime the streamwise velocity fluctuations u_{rms} monotonically increase, while the wall normal and spanwise components v_{rms} and w_{rms} monotonically decrease as DR is enhanced. Specifically, in the LDR regime the peak value of u_{rms} is increased to 3.5, while v_{rms} and w_{rms} decrease to almost half of their Newtonian magnitude. Further note that the peak locations of the u_{rms} shift away from the wall as %DR increases. This is consistent with the shift of the logarithmic region in the mean velocity profile. With increasing level of drag reduction (i.e., HDR/MDR regime), it can be seen that u_{rms} remains in the range of 3.5–4.0, while v_{rms} and w_{rms} decrease significantly. Although in the HDR/MDR regime the maximum value of u_{rms} does not changes significantly, it can be observed that the distribution becomes much broader near the peak position and the peak location is shifted further toward the center of the channel. Present prediction of the maximum value in u_{rms} in the HDR/MDR regime is in agreement with recent experimental observations of Ptasinski et al. [6].

4.2.3. Vorticity fluctuations

Fig. 12 shows typical vorticity fluctuations at various levels of drag reduction at $Re_\tau = 180$. The dimensionless (i.e., with respect to U_τ^2/ν) rms streamwise, wall-normal, spanwise vorticity fluctuations are shown in Fig. 12a–c, respectively. It can be seen that the intensity of the streamwise vorticity fluctuations monotonically decreases with increasing drag reduction up to MDR. It can also be clearly seen that the streamwise vorticity fluctuations for both the Newtonian and the drag reduced flow in the LDR regime show a characteristic local minimum followed by a local maximum. The locations of these minimum and maximum correspond to the average edge and center locations of the streamwise vortices (eddies) in the near wall

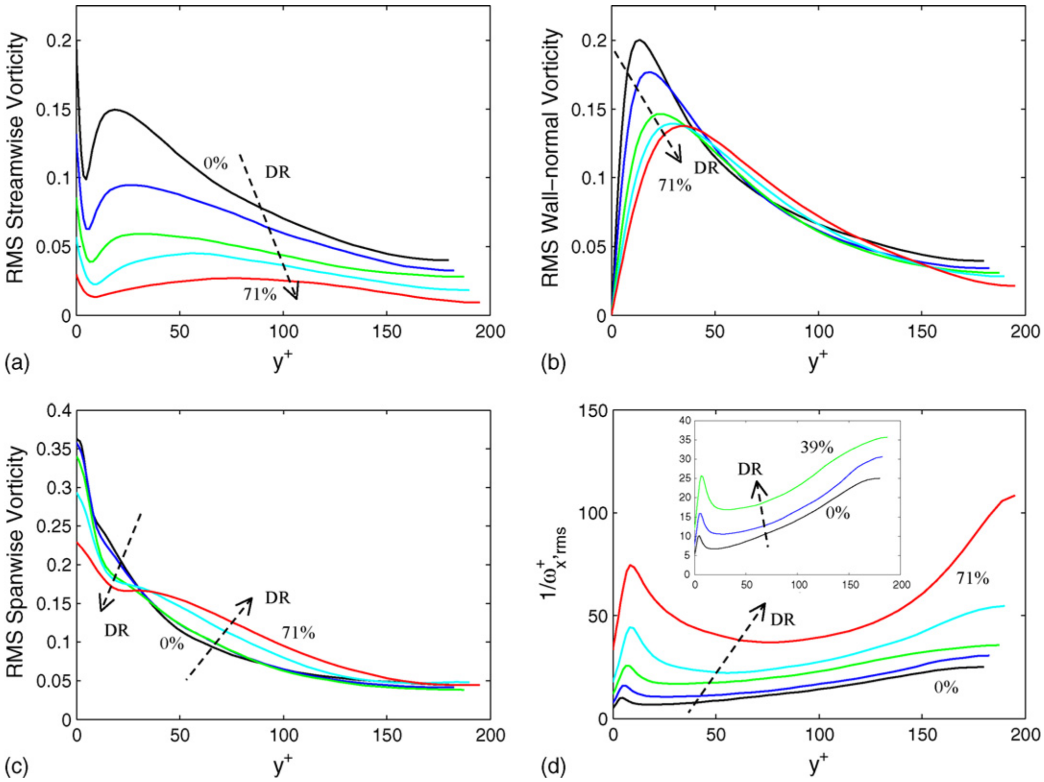

Fig. 12. The vorticity fluctuations as a function of the distance from the wall ($Re_\tau = 180$, %DR from 0%, 19%, 39%, 54%, to 71%). (a) $\omega_x{}^+{}_{,\text{rms}}$; (b) $\omega_y{}^+{}_{,\text{rms}}$; (c) $\omega_z{}^+{}_{,\text{rms}}$; (d) $1/\omega_x{}^+{}_{,\text{rms}}$.

region, respectively. The interval between these two locations is roughly proportional to the average size of streamwise vortices. As shown in Fig. 12a, the introduction of the polymer not only reduces the intensity of the fluctuations but also shifts the locations of both the minimum and the maximum towards the center of the channel. This implies a reduction in the intensity of the wall eddies and an increase in their average size (see Section 4.3 for details). It is widely accepted that a direct relationship between the streaky structures and the near wall streamwise vortices exists [22,24–26]. The mean streak spacing in Newtonian flows is approximately 100, however, an increase in the average streak spacing is observed in the LDR regime. Specifically, it has been shown that the streak spacing increase (in wall units) can be described as 0.19 × %DR in this regime [11,24]. As shown in Section 3, the streak spacing is a strong function of y^+ in the HDR and MDR regimes, hence, one cannot unambiguosly relate %DR to the average streak spacing.

In the HDR/MDR regime, the profiles of rms streamwise vorticity fluctuations are much flatter across the channel, and the locations of the minimum and maximum are not as obvious as in the LDR regime. Despite this fact, one can observe that the locations of the maximum are close to the center region of the channel, which indicates that the outer scales become important at large degrees of drag reduction. This is consistent with the theory of Screenivasan and White [29] at MDR who found that the length scales are of the order of the pipe radius. Hence, at high levels of drag reduction, the increase in the average streak spacing does not necessarily obey the linear correlation observed in the LDR regime.

The intensity of wall-normal vorticity fluctuations monotonically decreases with increasing drag reduction in the wall region, and the peak position is shifted to the center (see Fig. 12b). Further, as depicted in Fig. 12c, the intensity of spanwise vorticity fluctuations decreases with increasing DR in the near-wall region up to $y^+ \sim 30$, and subsequently increases in the outer region. This change is related to the enhancement of rms streamwise velocity fluctuations and decrease in wall-normal velocity fluctuations in the drag reduced flows.

Streamwise vortices play an important role in mediating the mass/momentum transfer between the near wall region and turbulent core by ejecting low-speed fluid from the near wall region to the core (ejection/upwash) as well as by bringing high speed fluid from the core towards the wall (sweep/downwash). Hence, it is of interest to examine the reciprocals of the streamwise vorticity fluctuations as it is a measure of the time scale associated with the dimensionless vortex rotation speed in wall units. Of particular interest is the relationship of this time scale to the polymer dimensionless time scale in wall units, i.e., We_τ. As shown in Fig. 12d this time scale increases with increasing drag reduction. It can also be seen that in the viscous sublayer and buffer layer for Newtonian flows, this time scale is in the range of 5–10 in wall units. If drag reduction is manifested when these time scales at small y^+ become equivalent (i.e., the dimensionless time scale for upwash and downwash become similar to We_τ), then one would expect that the onset of DR occurs in $5 \leq We_\tau < 10$. Indeed, this is consistent with the findings for the onset of drag reduction at $We_\tau = 6.25$ (i.e., Deborah number, $De = We_\tau \omega_x{}^+{}_{,\text{rms}} \sim O(1)$) [11,13].

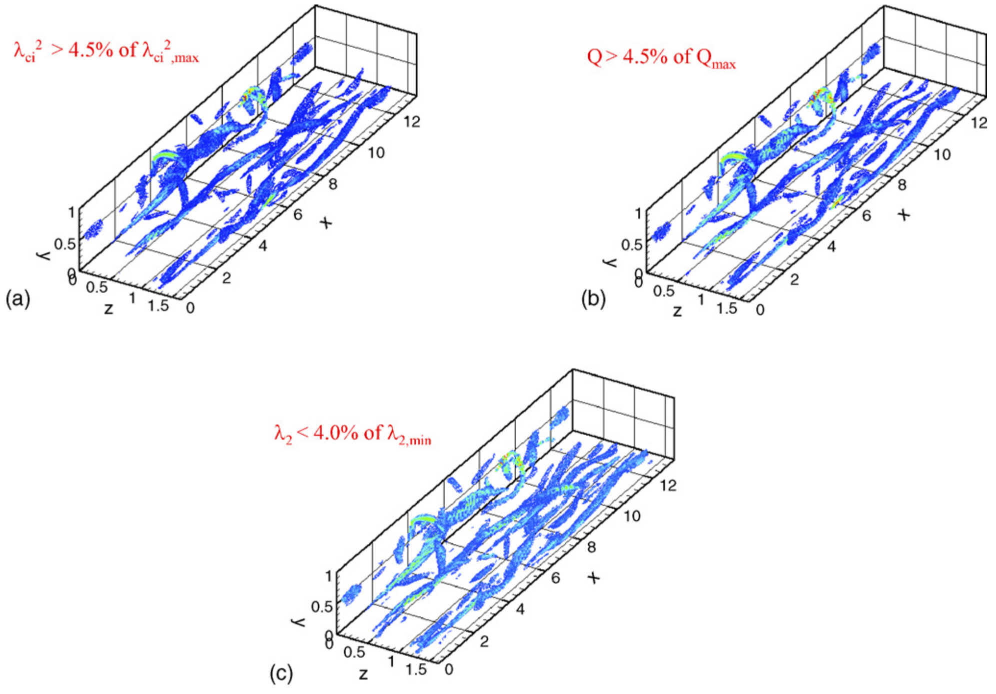

Fig. 13. Comparison of different vortex identification methods. (a) λ_{ci}^2-criterion [30], present study; (b) Q-criterion [31]; (c) λ_2-criterion [32].

This analysis clearly suggests that the near wall vortex time scale plays a significant role in determining the onset of DR. In fact, we have observed that this time scale plays a significant role in all regimes of DR. Specifically, at MDR (%DR = 71 at $Re_\tau = 180$, $We_\tau = 100$ and $L^2 = 14{,}400$ as shown in Fig. 12d) the first peak of this time scale is about 75, which is comparable to $We_\tau = 100$ required to achieve this MDR. We have also observed that for large L^2 (i.e., $L^2 \geq 3600$) over a broad range of %DR, We_τ $(\omega_x{}^+{}_{,\mathrm{rms}})_{\mathrm{peak}} \sim O(1)$ in the near wall region. This suggests that as elastic forces are enhanced they lead to stabilization of near wall axial vortices resulting in much longer and slower rotating vortices. Furthermore, these findings underline the fact that there is an intricate balance between elastic forces and average rotation speed of the near-wall axial vortices that determines upwash and downwash events and Reynolds stress production. It should be noted that our findings regarding the relationship between We_τ and $(\omega_x{}^+{}_{,\mathrm{rms}})_{\mathrm{peak}}$ in the near wall region for the DR onset and in the LDR regime for large L^2 are consistent with earlier DNS results [19] with the Oldroyd-B model.

4.3. Vortex identification and structure of turbulence

As mentioned above as DR is enhanced the intensity of near wall eddies is reduced and their average size in increased. In this section we provide direct evidence of this phenomenon via vortex visualization. A number of techniques for the identification of vortices have been proposed. In the present study we have applied the algorithm of Zhou et al. [30] using the isosurfaces of λ_{ci}, the imaginary part of the eigenvalue of the velocity gradient tensor $\nabla\mathbf{u}$ to visualize vortices. The isosurfaces of λ_{ci}^2 are plotted at an appropriate threshold. Note that within a few percent of the maximum value, the vortical structures are not a very sensitive function of the selected threshold value. Hence, a threshold value of approximately 5% is used in the present study. As pointed out by Zhou et al. [30], there are several advantages of this vortex identification method. For example, it is frame independent, hence the difficulty of choosing a proper frame of reference is eliminated. In addition, this method automatically eliminates regions having vorticity but no local spiraling motion, such as shear layers, because the eigenvalues are complex only in regions of locally circular or spiraling streamlines. The term λ_{ci}^2 is analogous to enstrophy, and it is also dimensionally consistent with other quantities used for vortex identification such as Q ($Q = 1/2\,(||\mathbf{\Omega}||^2 - ||\mathbf{S}||^2)$, where $\mathbf{\Omega}$ and $\mathbf{S}$ are the antisymmetric and symmetric parts of $\nabla\mathbf{u}$ [31]) and λ_2 (the second eigenvalue of the symmetry tensor $\mathbf{S}^2 + \mathbf{\Omega}^2$ [32]). The vortical structures obtained at MDR by these methods are shown in Fig. 13. It can be seen that these methods yield qualitatively identical and quantitatively similar results, provided a suitable threshold value is used. In the following we have used the λ_{ci}^2-criterion for vortex visualization.

Fig. 14 illustrates the dramatic modification of coherent vortical structures as drag reduction is achieved. It can be seen that the number of vortices is rapidly decreased with increasing %DR. This reduction is particularly significant at MDR. It can also be seen that with increasing %DR the number of axial vortices is significantly reduced, while the number of horseshoe-type vortices is increased (i.e., at MDR the horseshoe-type vortices are predominant). The weakening of the vortices has also been observed in the experiments (i.e., an increase of streak dimensions). At $Re_\tau = 125$ it can be seen that there are almost no axial vortices and the number of the horseshoe-type vortices are fewer

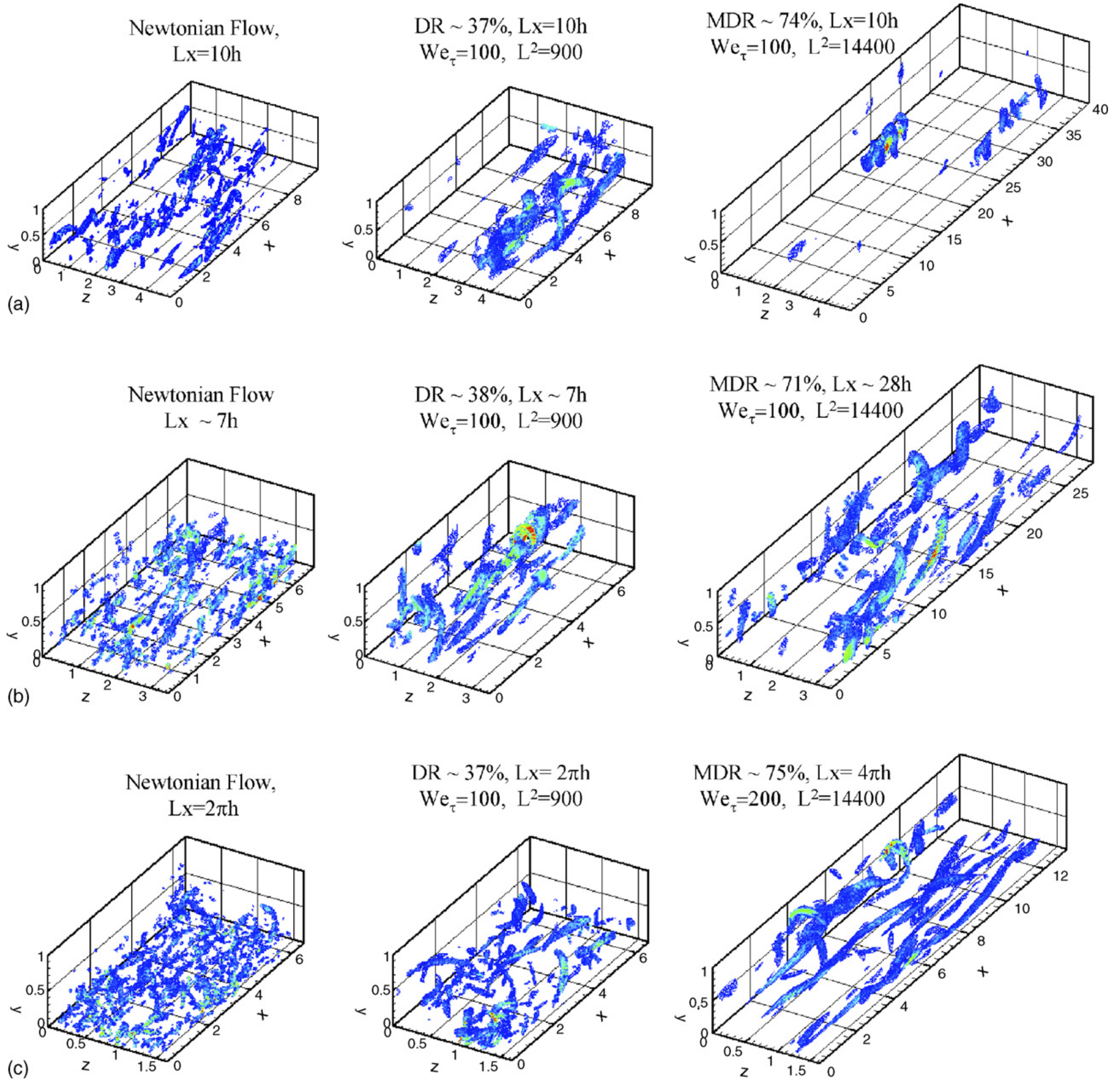
Newtonian Flow, Lx=10h

DR ~ 37%, Lx=10h We$_\tau$=100, L^2=900

MDR ~ 74%, Lx=10h We$_\tau$=100, L^2=14400

Newtonian Flow Lx ~ 7h

DR ~ 38%, Lx ~ 7h We$_\tau$=100, L^2=900

MDR ~ 71%, Lx ~ 28h We$_\tau$=100, L^2=14400

Newtonian Flow, Lx=2πh

DR ~ 37%, Lx= 2πh We$_\tau$=100, L^2=900

MDR ~ 75%, Lx= 4πh We$_\tau$=200, L^2=14400

Fig. 14. Vortex structure at various %DR. (a) $Re_\tau = 125$; (b) $Re_\tau = 180$; (c) $Re_\tau = 395$.

in comparison to higher Re_τ (i.e., 180 and 395). This provides another indication that the flow at $Re_\tau = 125$ in the HDR and MDR regimes is wall dominated.

The observed reduction in the intensity of the wall eddies provides evidence for the proposed mechanism of drag reduction based on the inhibition of the near wall eddies that facilitate significant amounts of the turbulence production. Mean flow oriented eddies are known to be responsible for 'ejecting' slowly moving fluid from the near wall region, resulting in the generation of low-speed streaks, a mechanism which eventually leads to the production of Reynolds stress [33,34]. Combining these observations with the decrease in $\omega_x{}^+{}_{,\mathrm{rms}}$ described earlier leads to the conclusion that the presence of macromolecules leads to inhibition of near wall vortices as well as a significant reduction in the rotation speed of vortices leading to a reduction in Reynolds stress production (i.e., DR).

4.4. Overall momentum balance

In a statistically stationary fully developed state, the total shear stress should follow a straight line. Specifically, the total shear stress is the sum of three contributions, namely, the Reynolds stress, the viscous stress of the solvent and the polymer stress. Since the simulations are performed with a constant pressure gradient, the total shear stress has the value τ_w at the walls and it is zero at the center of the channel. Normalized by wall stress $\tau_\mathrm{w}(=\rho U_\tau^2)$ the time averaged shear stress balance equation is given by [6,7,11]:

$$-\overline{uv} + \beta \frac{\mathrm{d}U}{\mathrm{d}(y/h)} + (1-\beta)\bar{\tau}_{xy} = 1 - \frac{y}{h} \tag{7}$$

where $-\overline{uv}$, $\tau_\mathrm{s} = \beta \frac{\mathrm{d}U}{\mathrm{d}(y/h)}$ and $\tau_\mathrm{p} = (1-\beta)\bar{\tau}_{xy}$ are the Reynolds shear stress, the viscous stress of the solvent and the polymer

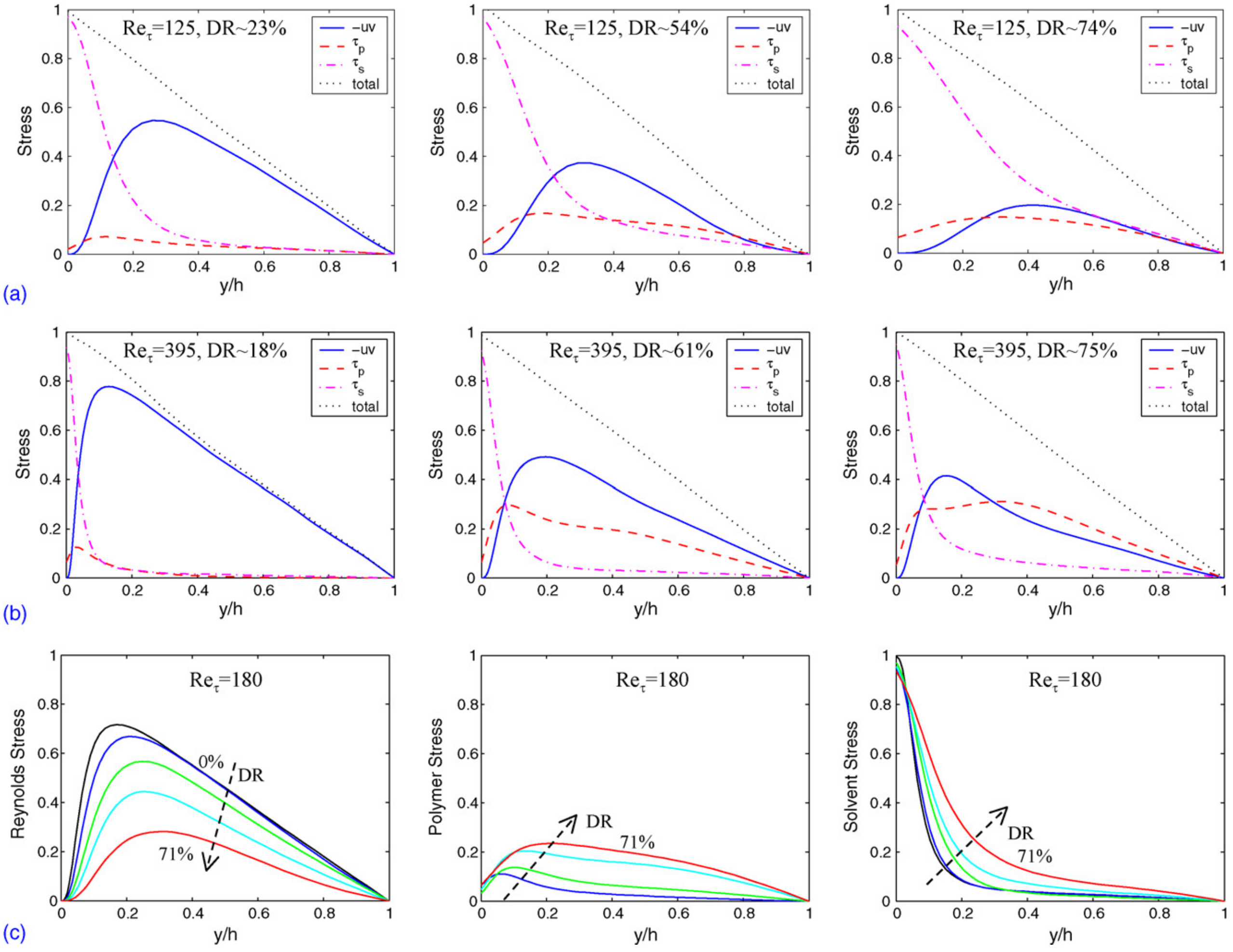

Fig. 15. Overall momentum balance. (a) $Re_\tau = 125$; (b) $Re_\tau = 395$; (c) $Re_\tau = 180$ (%DR from 0%, 19%, 39%, 54%, to 71%).

stress, respectively. τ_p is sometimes referred to as the Reynolds stress deficit due to the fact that the Reynolds shear stress and the solvent viscous shear stress do not add up to yield the expected linear distribution seen in Newtonian flows.

Various contributions to the overall shear stress balance as a function of the distance from the wall are shown in Fig. 15. In all cases the total shear stresses depict the expected linear profiles over the channel height, indicating that a stationary fully developed state has been reached. In the LDR regime, the polymer stresses increase monotonically with increasing drag reduction, while the Reynolds stresses decrease slowly. The polymer stress contributions are relatively small, and they occur mainly in the near wall region (i.e., the peak locations of polymer stress are in the buffer layer). However, as %DR in increased (i.e., HDR regime), the Reynolds stress is significantly reduced, and the polymer stress is comparable to the Reynolds stress. The increase in the polymer stresses and the decrease in the Reynolds stress are much less pounced as one moves from the HDR to the MDR regime. Specifically, at MDR the Reynolds stress is significantly reduced as compared to the LDR regime, but it remains non-zero. These observations are consistent with experimental results by Ptasinski et al. [6,7]. Moreover, at MDR the polymer stress on average has the same magnitude as the Reynolds stress, in fact the polymer shear stress is larger than the Reynolds shear stress in the near wall region. It can also be seen that at MDR and $\beta = 0.9$ the polymer stress contributions are about 10% of the total stress. Further note that the peak location of the Reynolds stresses shifts toward the channel center with enhanced drag reduction. At $Re_\tau = 125$ the solvent stress is significant over the entire channel height as opposed to higher Re_τ where it is limited to the near wall region. This is another indication that the flow is wall dominated at $Re_\tau = 125$ in the HDR and MDR regimes.

4.5. Polymer body force

A more rigorous approach for detecting the Reynolds stress deficit is to directly calculate the polymer stress. As shown in the RHS of momentum balance Eq. (2), the extra term added to the Navier–Stokes equation is the polymer body force [14,20]:

$$f_i = \frac{1-\beta}{Re_\tau}\partial_j \tau_{ij} \tag{8}$$

The body force term is clearly non-local and time varying and consequently, its local manifestation in the flow is quite complex. Hence, we are more interested in the polymer work $\overline{E_i} = \overline{u_i f_i}$

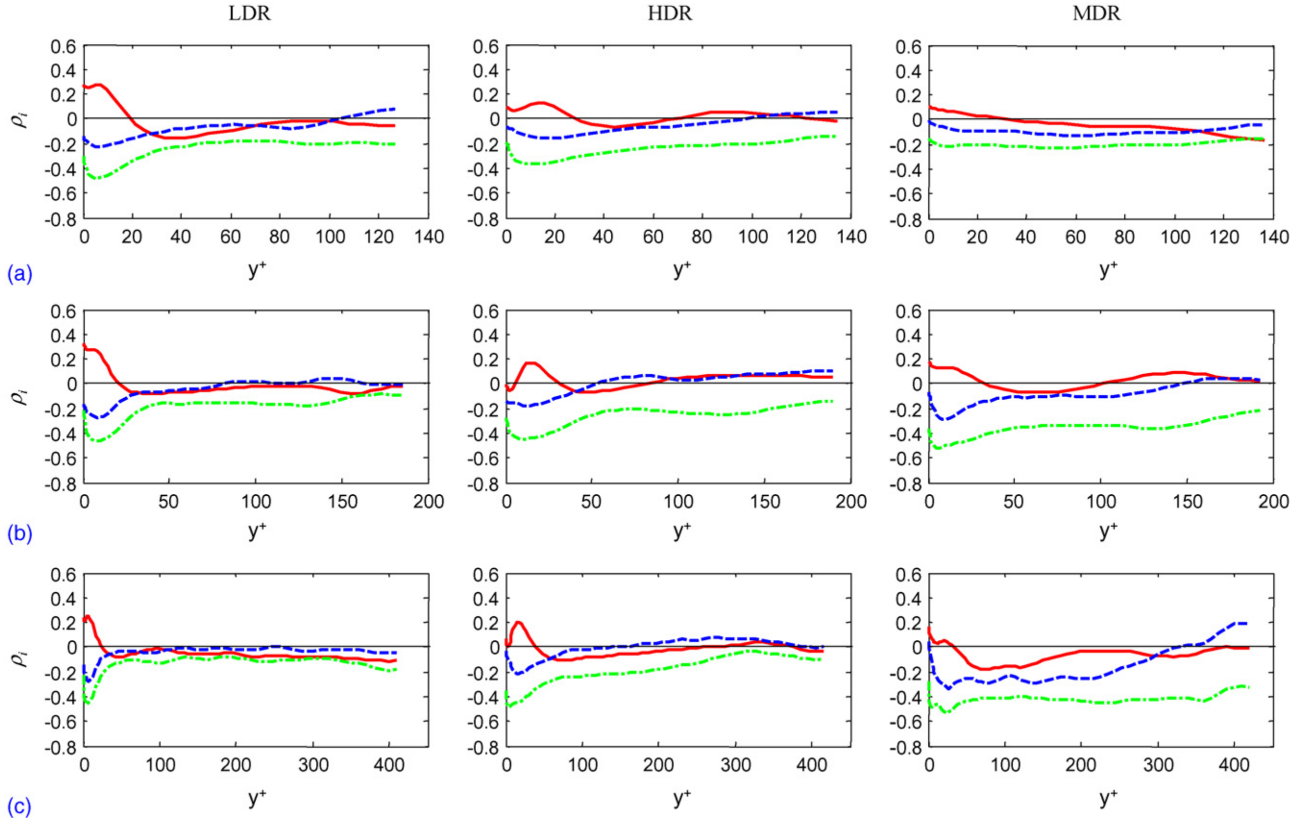

Fig. 16. The correlation between polymer body force and velocity fluctuations. (a) $Re_\tau = 125$; (b) $Re_\tau = 180$; (c) $Re_\tau = 395$.(—) ρ_x; (- - -) ρ_y; (-·-·-) ρ_z.

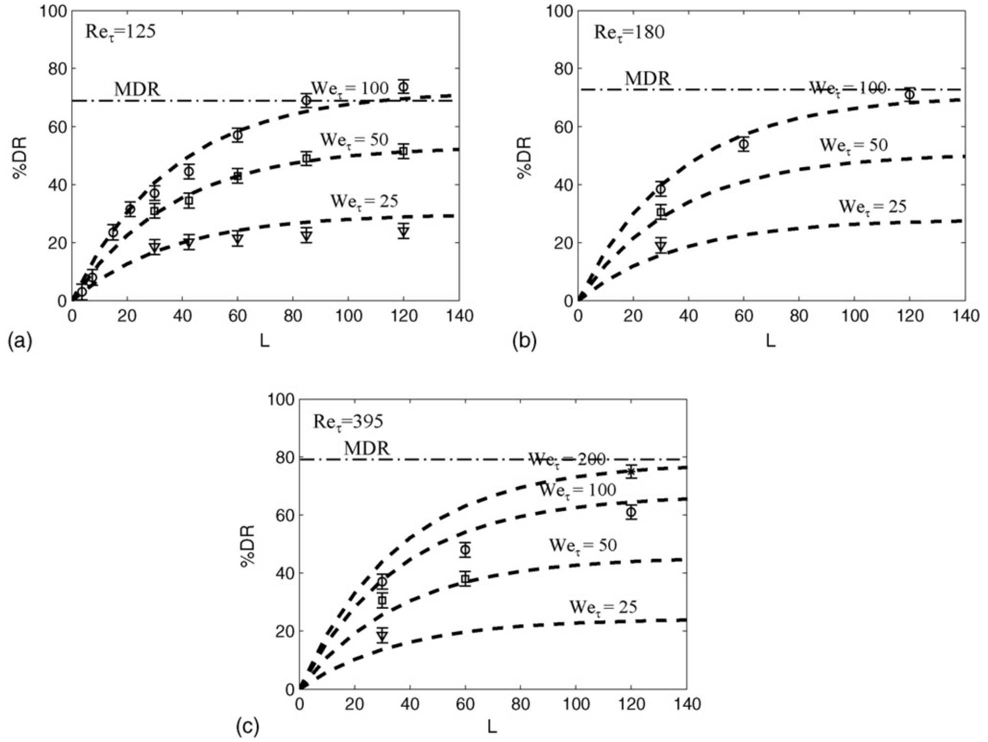

Fig. 17. The influence of polymer chain extensibility and Weissenberg number on the level of drag reduction. (a) $Re_\tau = 125$; (b) $Re_\tau = 180$; (c) $Re_\tau = 395$. (▽) $We_\tau = 25$; (□) $We_\tau = 50$; (○) $We_\tau = 100$; (*) $We_\tau = 200$. Dash lines represent Eq. (10).

(i.e., product of the velocity and polymer body force), because via the polymer work, the influence of polymer dynamics on the flow can be evaluated as it directly influences the budget of the turbulent kinetic energy. Specifically, if $\overline{E_i} < 0$ the energy carried by velocity fluctuations u_i could be dampened, otherwise it will be enhanced. Usually, the polymer work $\overline{E_i}$ is expressed in the correlation coefficient normalized by rms quantities:

$$\rho_i = \frac{\overline{u_i f_i}}{u_{i,\,\mathrm{rms}} f_{i,\,\mathrm{rms}}} = \frac{\overline{E_i}}{u_{i,\,\mathrm{rms}} f_{i,\,\mathrm{rms}}} \tag{9}$$

Therefore if the correlation ρ_i is positive (negative), the body force f_i has the tendency to increase (decrease) the fluctuation u_i, which is equivalent to positive (negative) work.

Fig. 16 shows the correlation between velocity fluctuations and polymer body force across the channel in all LDR, HDR and MDR regimes at various Reynolds numbers. Our results indicate that up to $y^+ \sim 20$–30, the polymer body force f_x and streamwise velocity fluctuation u are positively correlated, i.e. the viscoelastic force performs positive work on the u fluctuating velocity field, increasing u velocity fluctuations (i.e., enhanced u_{rms} as observed earlier). The correlations ρ_y and ρ_z are negative or very small close to zero across the channel. This explains the reduction of v_{rms} and w_{rms}. That is the polymers dampen vortices via negative $\overline{E_{\mathrm{y}}}$ and $\overline{E_{\mathrm{z}}}$. In general it can be observed that over a range of y^+ the correlations between polymer body force and velocity are negative. This supports the scenario where the polymer chains are extracting energy via stretching from the flow and hence reducing turbulent fluctuations. From Fig. 16, we can also see that within the Reynolds number range considered, the characteristics of ρ_i are the same, and with respect to the level of drag reduction same trends for ρ_i exist. Hence, we believe that these results are applicable in different DR regimes.

4.6. *Drag reduction scaling*

The percentage drag reduction (%DR) versus L, for $We_\tau = 25$, 50 and 100 at $Re_\tau = 125$, 180, 395 is shown in Fig. 17. It can be seen that the %DR as a function of L and We_τ at various Re_τ has a selfsimilar behavior. Moreover, the level of drag reduction tends to an asymptote at large L at fixed We_τ. Similarly, as L is fixed the %DR approaches an asymptote as We_τ in enhanced. This suggests that the influence of We_τ and L on %DR could be decoupled. Considering the fact that %DR reaches an asymptote as We_τ and L are enhanced, we have developed the following expressing for %DR as a function of We_τ, L and Re_τ

$$\%\mathrm{DR} = 80\left[1 - \mathrm{e}^{-\alpha(We_\tau - We_{\tau,c})(Re_\tau/Re_{\tau,r})^{-0.225}}\right]\left[1 - \mathrm{e}^{-\gamma L}\right] \tag{10}$$

where $\alpha = 0.025$, $\gamma = 0.0275$. $We_{\tau,\mathrm{c}}$ (=6.25) is the onset Weissenberg number. $Re_{\tau,\mathrm{r}}$ is the reference Reynolds number, and it is set to $Re_{\tau,\mathrm{r}} = 125$. The prefactor of 80 is used because at high We_τ and large L, the %DR at MDR asymptotes to 80% at high Reynolds numbers [4,8]. Eq. (10) explicitly shows that effective drag reduction requires large polymer extensibility L and high We_τ number. Our simulations also indicate that almost the same level of drag reduction can be obtained with FENE-P at $L^2 = 14{,}400$ and the Oldroyd-B ($L^2 \to \infty$) models. This clearly demonstrates that only at high Weissenberg numbers ($We_\tau \geq 100$) by enhancing the maximum chain extensibility MDR can be reached. A close examination of the figure clearly indicates that this scaling accurately describes the extent of DR in the HDR and MDR regimes. However, in the LDR regime deviations are observed. This suggests that perhaps in this regime (i.e., relatively small L values) the influence of L and We_τ cannot be decoupled.

5. Conclusions

Hi-Fidelity DNS of polymer induced drag reduction in turbulent channel flows up to the MDR limit have been performed. The polymeric stress is evaluated by the FENE-P and Oldroyd-B models. The influence of the friction Weissenberg number, chain extensibility and flow Reynolds number on the flow dynamics has been examined. It is shown that to obtain significant levels of drag reduction large polymer extensibility and high Weissenberg numbers are required. The simulation results in turn have been used to develop a scaling that describes the interplay between the rheological parameters (i.e., maximum chain extension and relaxation time) and the extent of DR as a function of Reynolds number. In addition, turbulence statistics have been analyzed and correlations between the polymer body force and velocity fluctuations have been developed with particular emphasis on the HDR and MDR regimes. Specifically, the interactions between polymer dynamics and flow modifications are elucidated. Our results indicate that in the near wall region, the polymer body force f_x and streamwise velocity u are positively correlated, i.e. the viscoelastic force performs positive work on the u velocity field, increasing u velocity fluctuations. While, The correlations ρ_y and ρ_z are negative or very small close to zero across the channel, indicating that the polymer chains are extracting energy via stretching from the flow and hence reduce turbulent fluctuations v_{rms} and w_{rms}. It has been observed that at large L^2 from the onset of DR to the MDR regime, $De = We_\tau\ ({\omega_x}^{+}{}_{,\mathrm{rms}})_{\mathrm{peak}} \sim O(1)$ in the near wall region. This suggests that there is an intricate balance between elastic forces and average rotation speed of the near-wall axial vortices that is a measure of the average time between upwash and downwash events and Reynolds stress production. Finally, a drag reduction scaling is deduced, as a function of Re_τ, We_τ and L. Specifically, in the HDR and MDR regimes the scaling accurately describes the extent of DR.

Acknowledgments

The financial support provided by DARPA (Grants MDA972-01-1-0007 and 29773A) is gratefully acknowledged. R.S. acknowledges useful discussions with Professors M.D. Graham, S. Balachandar and Fernando Pinho.

References

[1] J.W. Hoyt, The effect of additives on fluid friction, ASME J. Basic Eng. 94 (1972) 258–285.

[2] J.L. Lumley, Drag reduction by additives, Annu. Rev. Fluid Mech. 1 (1969) 367–384.

[3] J.L. Lumley, Drag reduction in turbulent flow by polymer additives, J. Poly. Sci. 7 (1973) 263–290.
[4] P.S. Virk, Drag reduction fundamentals, AIChE J. 21 (1975) 625–656.
[5] M.D. Warholic, H. Massah, T.J. Hanratty, Influence of drag-reducing polymers on turbulence: effects of Reynolds number, concentration and mixing, Exp. Fluids 27 (1999) 461–472.
[6] P.K. Ptasinski, F.T.M. Nieuwstadt, B.H.A.A. van den Brule, M.A. Hulsen, Experiments in turbulent pipe flow with polymer additives at maximum drag reduction, Flow Turbul. Combust. 66 (2001) 159–182.
[7] P.K. Ptasinski, B.J. Boersma, F.T.M. Nieuwstadt, M.A. Hulsen, B.H.A.A. Van den Brule, J.C.R. Hunt, Turbulent channel flow near maximum drag reduction: simulations, experiments and mechanisms, J. Fluid Mech. 490 (2003) 251–291.
[8] P.S. Virk, H.S. Mickley, K.A. Smith, The ultimate asymptote and mean flow structure in Toms' phenomenon, ASME J. Appl. Mech. 37 (1970) 488–493.
[9] P.S. Virk, Drag reduction in rough pipes, J. Fluid Mech. 45 (1971) 225–246.
[10] R. Sureshkumar, A.N. Beris, Effect of artificial stress diffusivity on the stability of numerical calculations and the flow dynamics of time-dependent viscoelastic flows, J. Non-Newtonian Fluid Mech. 60 (1995) 53–80.
[11] R. Sureshkumar, A.N. Beris, R.A. Handler, Direct numerical simulation of the turbulent channel flow of a polymer solution, Phys. Fluids 9 (1997) 743–755.
[12] C.D. Dimitropoulos, R. Sureshkumar, A.N. Beris, Direct numerical simulation of viscoelastic turbulent channel flow exhibiting drag reduction: effect of the variation of rheological parameters, J. Non-Newtonian Fluid Mech. 79 (1998) 433–468.
[13] K.D. Housiadas, A.N. Beris, Polymer-induced drag reduction: effect of the variations in elasticity and inertia in turbulent viscoelastic channel flow, Phys. Fluids 15 (2003) 2369–2384.
[14] E. De Angelis, C.M. Casciola, R. Piva, DNS of wall turbulence: dilute polymers and self-sustaining mechanisms, Comput. Fluids 31 (2002) 495–507.
[15] V.K. Gupta, R. Sureshkumar, B. Khomami, Polymer chain dynamics in Newtonian and viscoelastic turbulent channel flows, Phys. Fluids 16 (2004) 1546–1566.
[16] C.F. Li, V.K. Gupta, R. Sureshkumar, B. Khomami, Polymeric induced turbulent drag reduction: a mechanistic study, in: Proceedings of the XIVth International Congress on Rheology, Seoul, South Korea, 2004.
[17] C.F. Li, V.K. Gupta, R. Sureshkumar, B. Khomami, Turbulent channel flow of dilute polymeric solutions: drag reduction scaling and an eddy viscosity model, J. Non-Newtonian Fluid Mech. 139 (2006) 177–189.
[18] T. Min, H. Choi, Y.Y. Jung, Maximum drag reduction in a turbulent channel flow by polymer additives, J. Fluid Mech. 492 (2003) 91–100.
[19] T. Min, Y.Y. Jung, H. Choi, D.D. Joseph, Drag reduction by polymer additives in a turbulent channel flow, J. Fluid Mech. 486 (2003) 213–238.
[20] Y. Dubief, C.M. White, V.E. Terrapon, E.S.G. Shaqfeh, P. Moin, S.K. Lele, On the coherent drag-reducing and turbulence-enhancing behaviour of polymers in wall flow, J. Fluid Mech. 514 (2004) 271–280.
[22] T.S. Luchik, W.G. Tiederman, Turbulent structure in low-concentration drag-reducing channel flows, J. Fluid Mech. 198 (1988) 241–263.
[23] R.B. Bird, C.F. Curtiss, R.C. Armstrong, O. Hassager, Dynamics of Polymeric Fluids, vol. 2, Wiley, New York, 1987.
[24] D.K. Oldaker, W.G. Tiederman, Spatial structure of the viscous sublayer in drag-reducing channel flows, Phys. Fluids 20 (1977) S133–S144.
[25] W.G. Tiederman, T.S. Luchik, D.G. Boggard, Wall-layer structure and drag reduction, J. Fluid Mech. 156 (1985) 419–437.
[26] G. Hetsroni, J.L. Zakin, A. Mosyak, Low speed streaks in drag reduced turbulent flow, Phys. Fluids 9 (1997) 2397–2404.
[27] C.M. White, V.S.R. Somandepalli, M.G. Mungal, The turbulence structure of drag reduced boundary layer flow, Exp. Fluids 36 (2004) 62–69.
[28] K.D. Housiadas, A.N. Beris, Characteristic scales and drag reduction evaluation in turbulent channel flow of nonconstant viscosity viscoelastic fluids, Phys. Fluids 16 (2004) 1581–1586.
[29] K.R. Sreenivasan, C.M. White, The onset of drag reduction by dilute polymer additives, and the maximum drag reduction asymptote, J. Fluid Mech. 409 (2000) 149–164.
[30] J. Zhou, R.J. Adrian, S. Balachandar, T.M. Kendall, Mechanisms for generating coherent packets of hairpin vortices in channel flow, J. Fluid Mech. 387 (1999) 353–396.
[31] J.C.R. Hunt, A.A.Wray, P. Moin, Eddies, stream, and convergence zones in turbulent flows, Report CTR-S88, Center For Turbulence Research, 1988.
[32] J. Jeong, F. Hussain, On the identification of a vortex, J. Fluid Mech. 285 (1995) 69–94.
[33] S.J. Kline, W.C. Reynolds, F.A. Schraub, P.W. Runstadler, The structure of turbulent boundary layers, J. Fluid Mech. 30 (1967) 741–773.
[34] H.T. Kim, S.J. Kline, W.C. Reynolds, The production of turbulence near a smooth wall in a turbulent boundary layer, J. Fluid Mech. 50 (1971) 133–160.